

HETERODYNE DETECTION FIBER CONFOCAL
MICROSCOPE FOR IN VIVO SKIN IMAGING

by

Xiaohu Xue

A thesis submitted in partial fulfillment
of the requirements for the degree

of

Master of Science

in

Electrical Engineering

MONTANA STATE UNIVERSITY
Bozeman, Montana

January, 2011

©COPYRIGHT

by

Xiaohu Xue

2011

All Rights Reserved

APPROVAL

of a thesis submitted by

Xiaohu Xue

This thesis has been read by each member of the thesis committee and has been found to be satisfactory regarding content, English usage, format, citation, bibliographic style, and consistency and is ready for submission to the Division of Graduate Education.

Dr. David L. Dickensheets

Approved for the Department of Electrical and Computer Engineering

Dr. Robert C. Maher

Approved for the Division of Graduate Education

Dr. Carl A. Fox

STATEMENT OF PERMISSION TO USE

In presenting this thesis in partial fulfillment of the requirements for a master's degree at Montana State University, I agree that the Library shall make it available to borrowers under rules of the Library.

If I have indicated my intention to copyright this thesis by including a copyright notice page, copying is allowable only for scholarly purposes, consistent with "fair use" as prescribed in the U.S. Copyright Law. Requests for permission for extended quotation from or reproduction of this thesis in whole or in parts may be granted only by the copyright holder.

Xiaohu Xue

January, 2011

DEDICATION

To the friends and family who have supported me in achieving this goal. It is also dedicated to my advisor, Dr. David Dickensheets, who taught me that even the largest task can be accomplished if it is done one step at a time. Your motivation and support have been crucial to the realization of my goal in life, and continue to be a foundation for my future.

ACKNOWLEDGEMENTS

I would like to thank Dr. David Dickensheets for allowing me to take part in this project, for helping me improve my speaking, writing, technical and research skills, and for all the advice and patience he has given me in the past two years. His willingness to help with any and all problems I encountered during this project is greatly appreciated. I would like also like to thank: Chris Arrasmith for his tutoring in using the device and instrument when I started this project, Chunzi Zhang for his help in developing and debugging the electronics.

I would also like to express my appreciation to my family for helping me get the past several years. They have provided motivation and support to me all the time.

Funding Acknowledgement

This work was kindly supported by the National Institutes of Health. However, any opinions, findings, conclusions, or recommendations express herein are those of the author(s) and do not necessarily reflect the views of NIH.

TABLE OF CONTENTS

1. INTRODUCTION	1
Clinical Needs for Confocal Microscope.....	2
Optical Coherence Tomography.....	6
Heterodyne Detection.....	8
Thesis Organization.....	9
2. INSTRUMENT OVERVIEW.....	10
Confocal Laser Scanning Microscope System.....	10
Heterodyne Detection System.....	15
Optical Domain.....	16
Electrical Domain.....	21
Image Formation.....	25
3. OPTICAL DESIGN.....	28
Optical Layout.....	28
Zemax Simulation.....	32
First Telescope.....	32
Second Telescope.....	34
Objective Lens.....	38
Full System Layout.....	40
4. NOISE ANALYSIS.....	42
Direct Detection.....	43
Dynamic Range Analysis for Direct Detection.....	44
Heterodyne Detection.....	45
Dynamic Range Analysis for Heterodyne Detection.....	45
5. RESULTS.....	49
Optical Performance.....	49
Edge Response with Direct Detection using the APD.....	50
Axial Response with Direct Detection Using the APD.....	53
Edge Response with Heterodyne Detection.....	55
Axial Response with Heterodyne Detection.....	57
Noise Performance.....	59
Dynamic Range.....	59
Image.....	61
6. CONCLUSION.....	67

TABLE OF CONTENTS - CONTINUED

Future Work.....	69
REFERENCES CITED.....	70

LIST OF TABLES

Table	Page
2.1 MEMS driver interface	26
3.1 Properties of the MEMS scanning mirror	29
3.2 Comparison of 1st and 2nd configuration.....	38
4.1 Specification of C5460 module from Hamamatsu.....	43
4.2 Specification of PDB 130C module from Thorlabs.....	45
5.1 Theoretical and measured optical performance in direct detection	55
5.2 Theoretical and measured optical performance in heterodyne detection.....	59
5.3 Detected power with certain OD.....	63

LIST OF FIGURES

Figure	Page
1.1 Basic structure of skin layers	1
1.2 Wide-field versus point scanning of sample	3
1.3 The principal of confocal microscope.....	4
1.4 Image of mouse kidney	5
1.5 Image of a pollen grain	5
1.6 Diagram of a typical optical coherence tomography system	7
1.7 The principal of heterodyne detection	9
2.1 Laser wavelengths versus operating temperature	11
2.2 Principal of faraday rotator	12
2.3 Layout of a system with direct detection techniques	12
2.4 Quarter wave plate	13
2.5 Layout of heterodyne detection	15
2.6 Diagram of optical domain	16
2.7 Bragg diffraction.....	17
2.8 Frequency response of PDB130.....	19
2.9 Principal of 50-50 coupler	20
2.10 Diagram of electrical domain.....	21
2.11 Low pass filter reserves the baseband signal	22
2.12 Ramp, square and sine modulated signal and demodulated signal	23
2.13 Diagram of power splitter	24

LIST OF FIGURES - CONTINUED

Figure	Page
2.14 Typical performance for phase unbalance	24
2.15 The amplifier design	25
2.16 PEK turns on/off sequence.....	27
3.1 Photos of the MEMS scanning mirror	29
3.2 Beam profile.....	30
3.3 Block diagram of instrument subsystems	30
3.4 Optical setups of direct detection and heterodyne detection	31
3.5 Zemax layout for telescope lens simulation.....	33
3.6 Optical layout for the first telescope lens	34
3.7 Optimization for beam width.....	36
3.8 1 st and 2 nd configuration for telescope lens design	37
3.9 1 st configuration and wavefront map for on-axis and off-axis ray.....	37
3.10 2 nd configuration and wavefront map for on-axis and off-axis ray.....	38
3.11 Paraxial objective lens	39
3.12 Optical performance for paraxial lens combined with hemisphere lens.....	40
3.13 Layout of the complete system	41
3.14 Spot diagram for the final design.....	41
4.1 The power distribution of 50/50 coupler	46
4.2 Dynamic range comparisons of direct detection and heterodyne detection	47

LIST OF FIGURES - CONTINUED

Figure	Page
5.1 Normalized edge response of direct detection	51
5.2 A letter 'E' on the object is used to represent an edge.....	52
5.3 Calibrated oscilloscope trace	52
5.4 Normalized axial response curves	53
5.5 Measured result of axial response.....	54
5.6 Normalized edge responses.....	56
5.7 Measured edge response of heterodyne detection with log detector	56
5.8 Theoretical axial responses.....	57
5.9 Measured axial response in heterodyne detection with log detector	58
5.10 Measured dynamic range of direct detection.....	60
5.11 Measured dynamic range of heterodyne detection	60
5.12 Example images of heterodyne detection	61
5.13 Images with OD 0, OD 1.6 and OD 4 in direct detection.....	62
5.14 Images with OD 0, OD 1.6, OD 4 and OD 8 in heterodyne detection	62
5.15 Tissue images with direct detection and heterodyne detection.....	64
5.16 Images taken using direct detection.....	64
5.17 Images taken using heterodyne detection	65

ABSTRACT

Confocal microscopy has been demonstrated to be a very effective tool for imaging in-vivo samples. The confocal imaging geometry provides a dramatic optical advantage for microscopy by discriminating against out-of-focus background with minimal loss of image-forming signal. Because of these advantages, the confocal laser scanning microscope (CLSM) can image a thin layer clearly from a thick sample without biopsy. However, current usage of CLSM is limited by the signal-to-noise ratio using conventional optical detection. In order to achieve deeper penetration into the skin in a clinical setting, a technique called heterodyne detection is incorporated into the CLSM system. This thesis describes the optical, mechanical and electrical design of the system, evaluates system noise and imaging performance, and provides initial skin images collected by the heterodyne system, comparing the results with direct detection. The heterodyne detection system is proved to have deeper penetration than the direct detection system, but the image quality is degraded.

INTRODUCTION

With thousands of new cases diagnosed annually, skin cancer is the most common cancer form in the United States. Research shows that 40%-50% of people who live to age 65 will get skin cancer at least once [1]. Each year more than 3.5 million cases in 2 million people are diagnosed [2]. Each year new cases of skin cancer are found more than the combined incidents of cancers of the breast, prostate, lung and colon. Although skin cancer is prevalent, most types of skin cancer are not fatal. With early diagnosis and proper recovery procedure, the probability of acquiring skin cancer can be highly reduced [3].

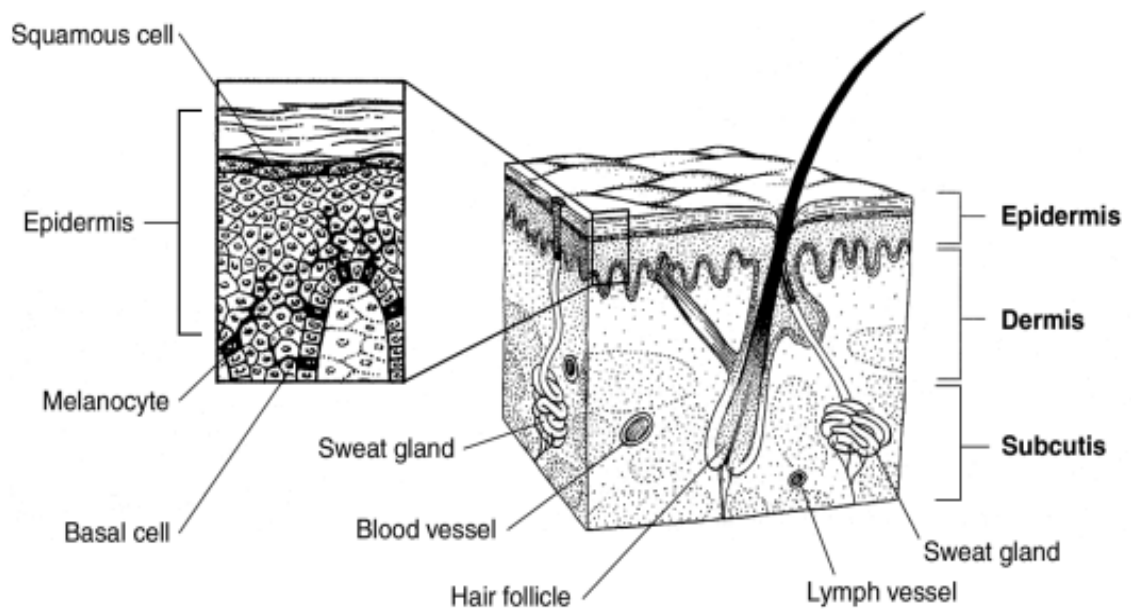


Figure 1.1 Structure of skin layers [4]

Figure 1.1 shows the basic structure of skin layers. Basal cells and Melanocyte cells are all located at the epidermis-dermis junction, so a cancer cell diagnosis instrument should be able to penetrate through the epidermis and into the dermis [4].

Skin cancer typically affects three different types of cells in the epidermis, known as basal cells, squamous cells, and melanocytes. Basal cells are the bottommost epidermal cells that lie along the junction between the epidermis and dermis. Basal cell carcinoma (BCC) is the most common form of skin cancer; annually approximately 2.8 million cases are diagnosed. Although BCC is not fatal, it causes extreme disfiguring. Squamous cell carcinoma (SCC) is the second most common form. An estimated 700,000 cases are diagnosed annually, which result in 2,500 deaths. Melanoma accounts for about only 3% of skin cancer cases, but it leads to 75% of skin cancer death [5].

Clinical Needs for Confocal Microscope

The data above shows the need for an effective tool in skin cancer diagnosis. Traditionally, skin cancer diagnosis starts with visual inspection, usually supported by a dermoscope. If a suspect lesion is determined, a biopsy is taken for further diagnosis which usually takes 1-2 weeks. Inaccuracy and ineffectiveness arises because of the visual similarities between many benign skin lesions and malignant cancers. More than 1 billion dollars are used for the treatment of skin cancer every year, but the correct visual diagnosis rate is only 50% to 75% for experienced clinicians [6]. The inaccuracy and ineffectiveness leads to not only unnecessary cost but also the discomfort of the patient. The confocal microscope has the potential to perform real time in vivo diagnosis, with

higher diagnosis accuracy, as well as increased patient comfort. The confocal microscope has several advantages over a conventional wide-field optical microscope, which makes it more and more useful in clinical usage. The confocal property permits imaging of thin optical sections in thick samples.

In a conventional wide-field microscope, the entire specimen is viewed in light from a light source. All parts of the specimen are excited by the light source and the image is formed. The image can be viewed either by eye or captured by an imaging device [7].

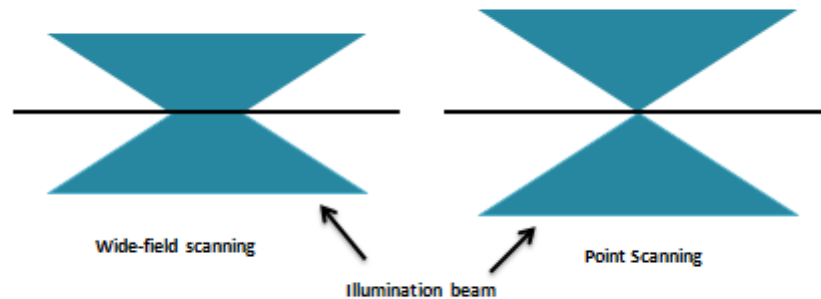


Figure 1.2 Wide-field versus point scanning of sample

The method of image formation in a confocal microscope is basically different. The illumination is acquired by scanning focused beams of light through the specimen. A laser is usually used in this scan. The images obtained by scanning the specimen in this way are called optical sections. This term refers to that the images collected with the noninvasive method, using focused beam instead of physical means to section the

specimen [7]. In addition, unlike the conventional wide-field microscope which detects not only the scattered signal from the focal plane but also the signal out-of-focus, confocal microscope system can only see the signal from the focal plane due to an aperture which blocks the out-of-focus signal and background light. Refer to Figure 1.3 for the principal of confocal microscope. The solid line represents the beam from the light source and reflected beam which is collected by a light detector. The dashed line represents the beam reflected from the object but not from the focal plane. Due to the existence of an aperture, most out-of-focus light is not collected by the light detector. Although some of the out-of-focus light enters the light detector, it is not strong enough to be seen. In this manner, the confocal microscope can collect only the data from within the focal plane. Figure 1.4 shows the image of mouse kidney which shows the contrasting enhancement. Image on the left is under a conventional microscope and image on the right is under a confocal microscope.

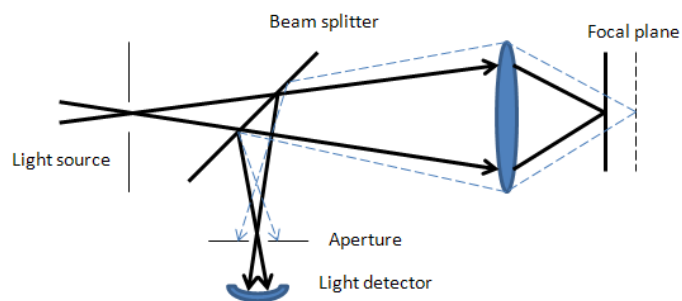


Figure 1.3 The principal of confocal microscope

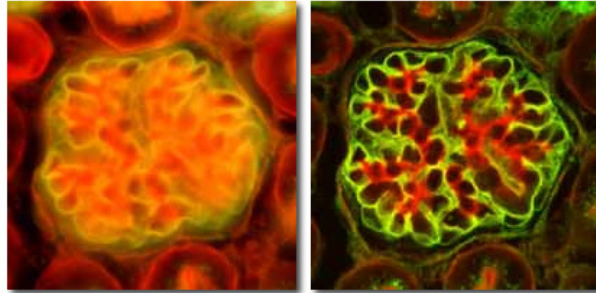


Figure 1.4 Image of mouse kidney (With permission from MicroscopyU) [7]

As discussed above, the most important component of the scanning unit is the pinhole aperture. The aperture functions as a spatial filter at the conjugate image plane located in front of the sensor [7]. Usually, the size of the pinhole is adjustable, which is used to operate the optical sectioning thickness. The pinhole aperture also serves to eliminate much of the stray light passing through the optical system. In a fiber-based CLSM system, the adjusting ability is achieved by using optical fiber with different core size, which will be discussed specifically in a later chapter.

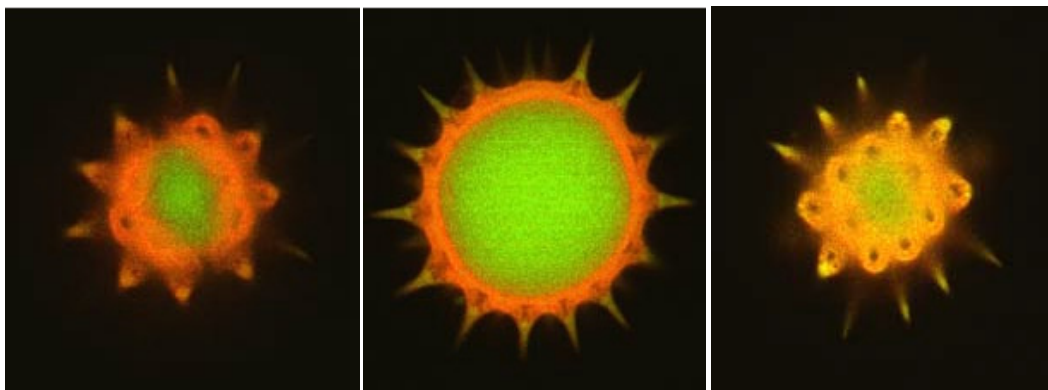


Figure 1.5 Image of a pollen grain (With permission from MicroscopyU) [7]

Another feature of the confocal laser scanning microscope is that it enables 3-dimensional image reconstruction. Thicker specimens can be imaged layer by layer by translating the objective lens along the optical z axis of the confocal microscope. Figure 1.5 shows the serial sectioning of a pollen grain from three different layers.

Optical Coherence Tomography

Confocal microscopy owns several advantages over wide-field microscopy from what has been discussed, however it is limited to relatively transparent specimens or shallow penetration condition, since image contrast is degraded by light scattering and aberrations. Optical coherence tomography (OCT) is widely used to improve confocal microscopy when image is taken on highly scattering tissue like skin. The improved signal sensitivity offered by interferometric detection can offer the ability of an OCT system to image structures in tissue beyond the limit of conventional wide-field and confocal microscopes. For transparent tissues, OCT system can image more than 1cm. In highly scattering tissues like skin, OCT can image the structure like subcutaneous tissue and blood vessels 1-2mm beneath the surface. This is because when the penetration goes deeper, the amount of light escape besides the scattering light is not strong enough to be detected [8].

The core component in an OCT system is an interferometer, which splits a laser source field into a reference field E_r and sample field E_s . The sample field focuses through the optical system and objective lens to a certain point below the surface of the tissue. The reflected sample field E'_s , which contains the information of the tissue, is

mixed with reference field E_r on the photodetector. After proper signal processing, the field on the sample can be reconstructed and the image is rendered accordingly. Depth selection is achieved by setting the reference arm length to match the desired sample arm depth, relying on the short coherence length to discriminate the desired back reflected light from the rest of the scattered field. OCT is typified by low numerical aperture optics, and has resolution that is usually at least 10 times worse than confocal microscopy.

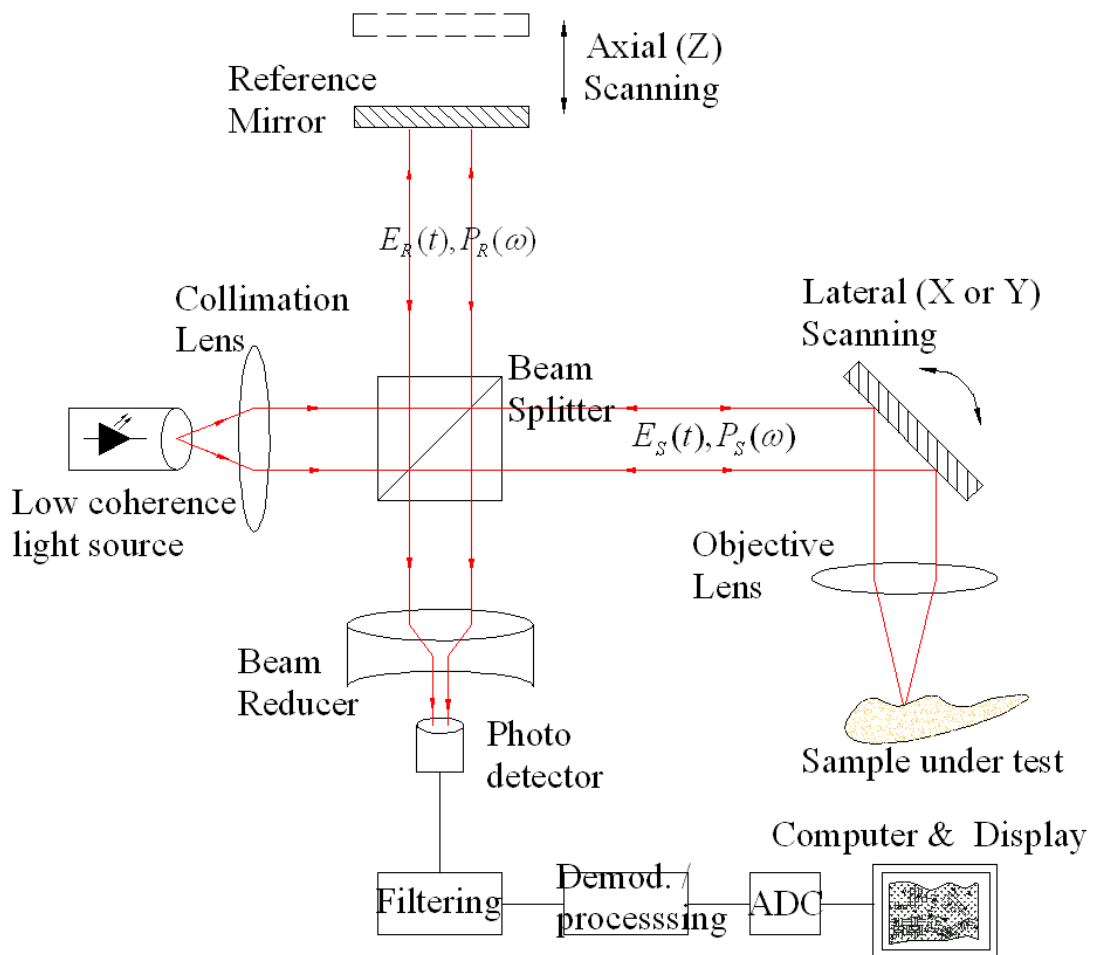


Figure 1.6 Diagram of a typical optical coherence tomography system [8]

Heterodyne Detection

Optical heterodyne techniques can be categorized as a special case of OCT. It is often combined with laser scanning and applied to coherent light fields. Like a typical OCT system which has an interferometer, the heterodyne system is actually an interferometric system. The major difference between the heterodyne system and the OCT system is the reference beam, also known as a local oscillator beam, which is frequency shifted by an acoustic-optical modulator (AOM). The signal beam and the reference beam are superimposed at the photodetector. The major reason that we are investigating the heterodyne detection system is that the heterodyne detection system has larger dynamic range and better noise performance than the direct detection system. The dynamic range of the heterodyne detection system is estimated to be 30dB more than the direct detection system. This allows deeper penetration in the skin and therefore may offer more accurate diagnosis. Unlike OCT, our system still uses a confocal arrangement with large numerical aperture to achieve high optical resolution, and has a light source with long coherence length. Interferometric detection is used only to improve the sensitivity, and is not the mechanism for depth discrimination.

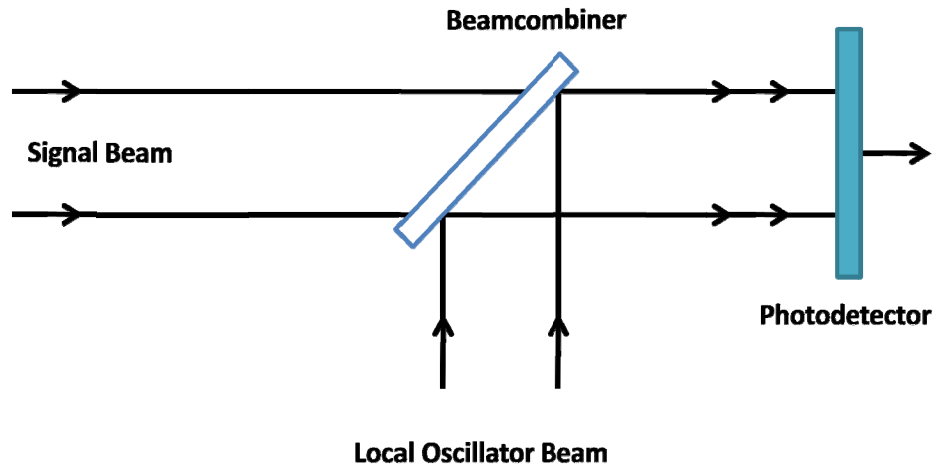


Figure 1.7 The principal of heterodyne detection

Thesis Organization

This thesis will discuss the design, setup and performance of the confocal laser scanning microscope with heterodyne detection system. In chapter two, an overview of the instrument will be given discussing the various sub systems in the design. Chapter three will describe the optical design including the optical layout, Zemax modeling and choices of lenses in the microscope. Chapter four includes the noise analysis of the heterodyne detection compared with the direct detection. Results from evaluation of the optical system and sample images will be presented in chapter five. Chapter six is the conclusion chapter which will also discuss necessary improvements for future development for this system.

INSTRUMENT OVERVIEW

The confocal laser scanning microscope with heterodyne detection can be divided into three sub systems: confocal laser scanning microscope system, heterodyne detection system, and the image forming system. Currently, the system is a bench-top system, so the size of the system is not minimized yet.

A brief review of the confocal laser scanning microscope system will be presented in the beginning of this chapter, and then the heterodyne detection will be introduced compared with the previous direct detection techniques, followed by a description of the image forming system including the synchronization and amplification electronics plus the A/D converter, also known as the frame grabber.

Confocal Laser Scanning Microscope System

To illuminate of the structure to the required depth, a wavelength in the near IR was selected. Also, because of the scattering loss, the light reflected is very weak and also proportional to the input laser power, so a laser with high emission power is needed. Plus, the laser power should be adjustable to avoid saturation. A SANYO laser diode was chosen which has 100mW maximum power. Figure 2.1 shows a plot of laser wavelength as a function of operating temperature. In order to maintain the laser at its wavelength, a temperature controller is needed.

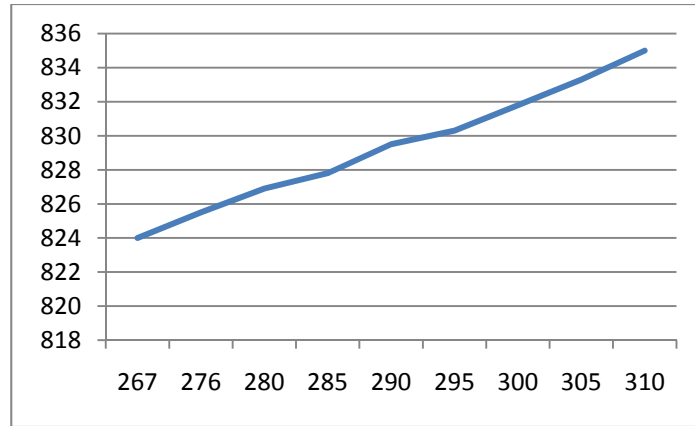


Figure 2.1 Laser wavelength (in nm) versus operating temperature (in K)

Figure 2.3 shows the layout of a system with direct detection techniques. The broader line shows the forward beam while the narrow line represents the backward beam. The laser source passes through a half wave plate which is used to control the polarization orientation of the output beam. For heterodyne detection we control polarization to manipulate the amount of light sent as the signal beam or the reference beam through a polarization beam splitter. In the direct detection case, the half wave plate is adjusted to maximize the light sent to the sample and minimize the light sent to the reference arm (the reference arm is not used for direct detection). In the heterodyne detection case, about 10% percent of the total amount is sent to the reference arm. Even though this is a small amount of light, compared to the weak response from the skin, it is sufficient to be a reference beam and is dominant at the detector.

A faraday rotator is placed for the purpose of changing the polarization state of the incident beam. The incident beam which passes through the polarization beam splitter is horizontally polarized. When the beam goes through the faraday rotator, its

polarization state is rotated by 45° clockwise. Before the reflected beam enters the faraday rotator, it has the same polarization state as shown in figure 2.2. When the beam goes through the faraday rotator, its polarization state is rotated by 45° in clockwise again. The resulting vertical polarization state will cause the reflection of the beam at the polarization beam splitter. This scheme avoids the beam reflecting back to the laser cavity which may make the laser source unstable, and directs the reflected light to the detection fiber. This arrangement is often called an optical circulator.

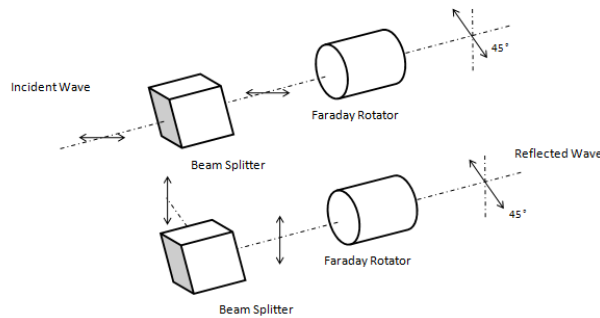


Figure 2.2 Principal of faraday rotator

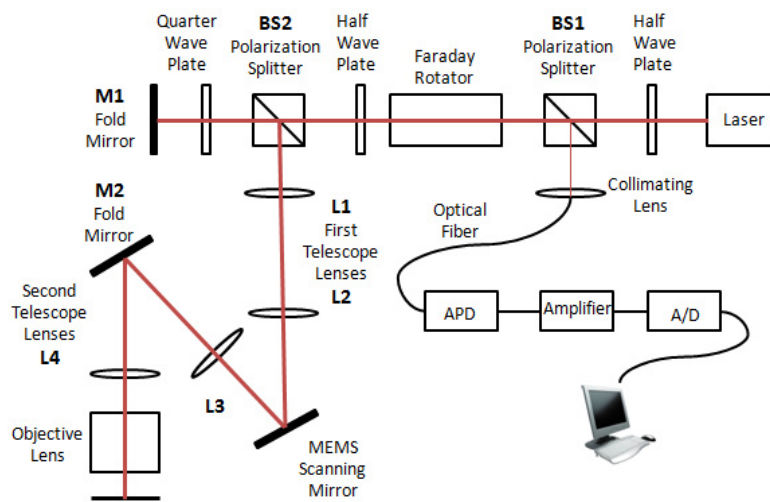


Figure 2.3 Layout of a system with direct detection techniques

Another half wave plate is used to change the polarization state of the signal beam back to the horizontal polarization state again in order to maximize the light that goes into the system. This beam passes through beam splitter BS2 and then a quarter wave plate to fold mirror M1. Figure 2.4 shows the principal of the quarter wave plate. Quarter wave plate is used to change the polarization state of the beam reflected from the mirror. Once the beam passes through the quarter wave plate, the polarization state is changed from a horizontal polarized state to a circular polarized state; after reflecting back from a fold mirror and passing through the quarter wave plate again the polarization state of the signal beam is changed from the circular polarized state to vertical polarized state thus it will all reflect at the polarization beam splitter.

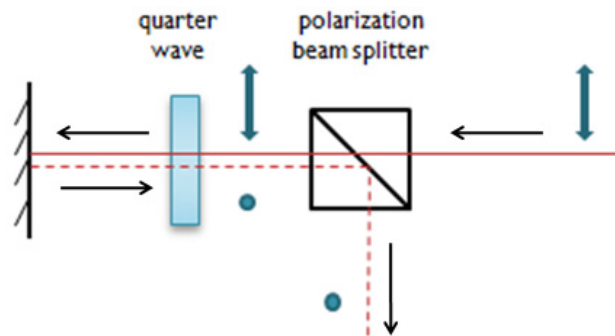


Figure 2.4 Quarter wave plate

The location where a fold mirror sits will be eventually replaced by a focus control MEMS mirror. The MEMS mirror has the ability of focus control based on variable curvature with electronic control and is a key point in shrinking the size of the whole system. In the previous handheld CLSM (using direct detection), focus control is

achieved by mounting the objective lens to a translation stage [9]. By translating the objective lens, the confocal system is able to adjust for focus control. Due to the limitation of mechanical adjustment like translation speed and additional complexity, the new focus control technique will be incorporated into the miniature heterodyne detection system in the future.

Next, the signal beam passes through a telescope to adjust the size of the beam to the MEMS scanning mirror. The collimated beam from the laser has a 3.3 mm diameter, while the pupil in the MEMS scanning mirror only has 1mm diameter. In addition to the reason that the telescope lens is used to shrink the size of the beam, the telescope lens is also used as an optical relay to make an image of the MEMS focus control mirror on the MEMS scanning mirror, The MEMS scanning mirror offers potential to make the whole system portable due to its small size compared to a galvanometer. Another pair of lens L3 and L4 form a telescope to provide a magnification of three times to ensure the laser beam fills the rear aperture of the objective lens. The telescope also images the MEMS mirror into the rear aperture of the objective lens. Two different objective lenses can be incorporated into the system to provide various numerical apertures (NA) for imaging quality testing. Either a clear aperture or a hemisphere lens can be placed between the objective lens and the skin. The hemisphere lens can have an additional increase in NA to improve resolution and cross-sectioning ability.

The scatted light from the sample will return on the same route as the light passes in the forward direction. The only difference is that the faraday rotator rotates 90° compared to the original beam, thus the beam will all reflect on the polarization beam

splitter and then be coupled into a fiber and finally detected by an Avalanche Photo Diode (APD) for direct detection. The electrical signal will be amplified then sent to an A/D converter (frame grabber). Given proper horizontal and vertical synchronization signal, from the user interface, an image will be constructed. This is the general principal of a direct detection approach.

Heterodyne Detection System

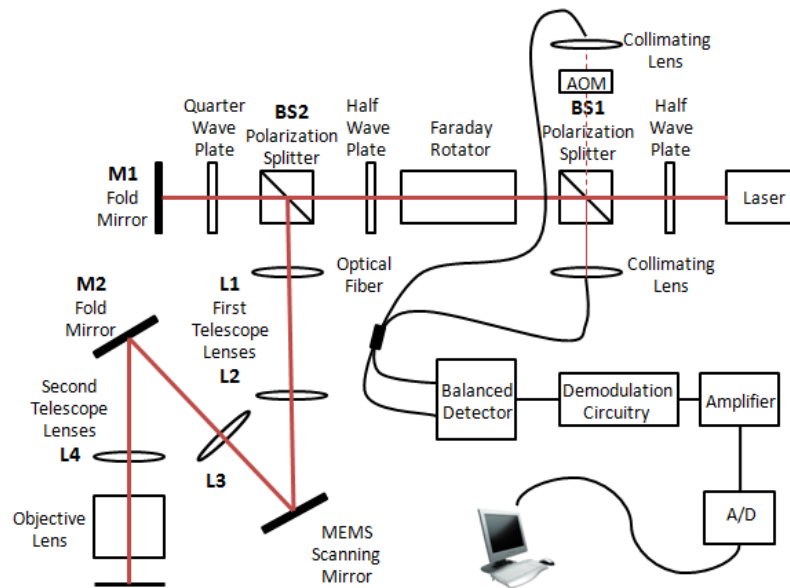


Figure 2.5 Layout of heterodyne detection

The heterodyne detection system is built based on the previous direct detection system as shown in Figure 2.5. The beam to be detected is still coupled into the fiber; however in the heterodyne detection setup the detected signal will be mixed with another beam to construct an interferometric system. This beam is the reference beam that has been discussed in the introduction chapter. Initially, the beam has the same optical

frequency as the signal beam. When the beam is incident on an acousto-optic modulator (AOM) from the Bragg angle it diffracts from the traveling acoustic wave. The diffracted beam therefore has a frequency shift based on the driving signal of the acousto-optic modulator. In this system, the optical frequency has a 40MHz shift.

By doing this, two advantages can be taken. First, a 40MHz carrier frequency will allow a signal bandwidth as high as 20MHz. Second, a signal running at a high frequency is less vulnerable to the pink noise. Pink noise, often referred to as $1/f$ noise, is a signal or process with a frequency spectrum such that the power spectral density is inversely proportional to the frequency.

The heterodyne system can be divided into two domains: optical domain and electrical domain. The balanced detector served as a transducer from the optical domain to the electrical domain.

Optical Domain

The optical domain of the heterodyne detection is shown in Figure 2.6.

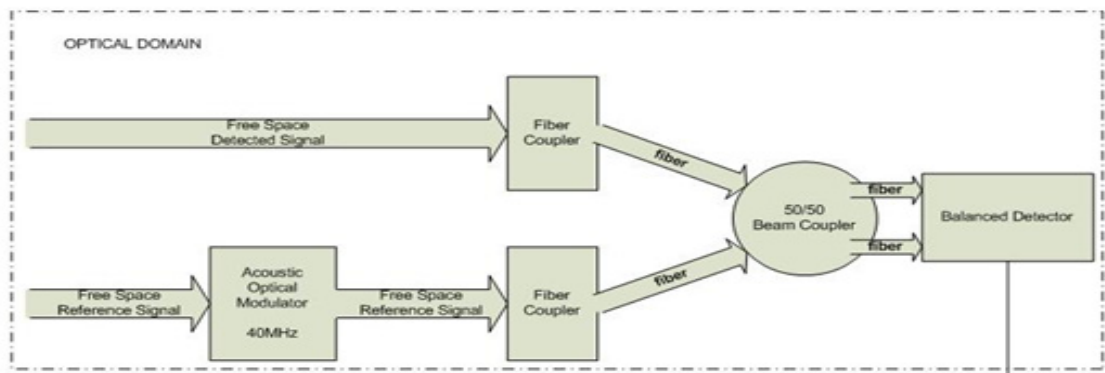


Figure 2.6 Diagram of optical domain

An acousto-optic modulator (AOM), also known as a Bragg cell, uses the acousto-optic effect to diffract and shift the frequency of light using sound waves (usually at radio-frequency).

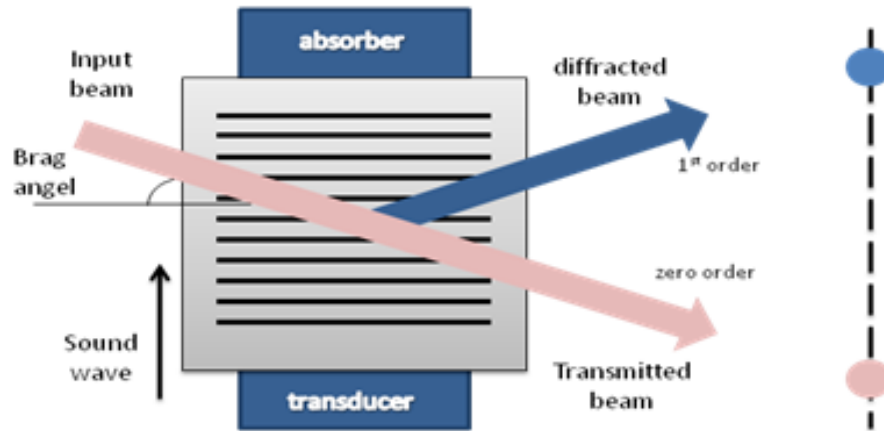


Figure 2.7 Bragg diffraction

Figure 2.7 shows the Bragg diffraction: an acoustic plane wave acts as partial reflector of light, more efficient when the angle of incidence θ satisfies the Bragg condition.

$$\sin \theta_B = \frac{\lambda}{2\Lambda} \quad \text{Bragg Condition} \quad (2.1)$$

λ is the wavelength of light in the material and Λ is the wavelength of sound. In our system $\lambda=523\text{nm}$, $\Lambda=16.6\mu\text{m}$ and θ_B is 0.9° . This angle is inside the medium, since the cell is placed in air, external angle is 1.5° .

The model we use is an ISOMET OAM1141-T40-2 which is specifically designed for operation as a 40MHz acousto-optic frequency-shifter at 633nm. For the

830nm laser source we use, the module which is coated for 633nm has more insertion loss, but still less than 3%, which is acceptable for our application.

The reference signal and the detected signal are coupled into two input ports of a 50-50 coupler with polarization maintaining fiber. Since the heterodyne system is intrinsically an interferometer, two arm length needs to be balanced. A small difference of the length of two arms can be allowed, but should be less than coherence length of the laser source used in the system. Two output arms are connected to the inputs of a balanced detector. The optical signal is thus converted to the electrical signal.

The Newport F-PMC-780-50 Polarization Maintaining (PM) Fiber Optic Coupler is chosen for this system which utilizes evanescent wave coupling to provide a fixed 50/50 ratio 2x2 coupler, with high polarization extinction ratio (from -24dB to -27dB) and low insertion loss (typically 0.05dB) and small back reflection (< -65 dB) for the 780 nm wavelength. We observe acceptable behavior when using 830 nm light as well. Due to there is no deformation in the wave-guide cores, this coupler enjoys inherent advantages. In addition, these PM fiber couplers are more resistant to aging and environmental effects because the two Panda fiber halves are placed in direct contact with each other. The F-PMC comes in a small, specially designed silicone rubber package that allows low stress contact of the fiber halves over a broad range of temperatures. The couplers come standard with 1 meter fiber pigtails and FC/APC connectors [10].

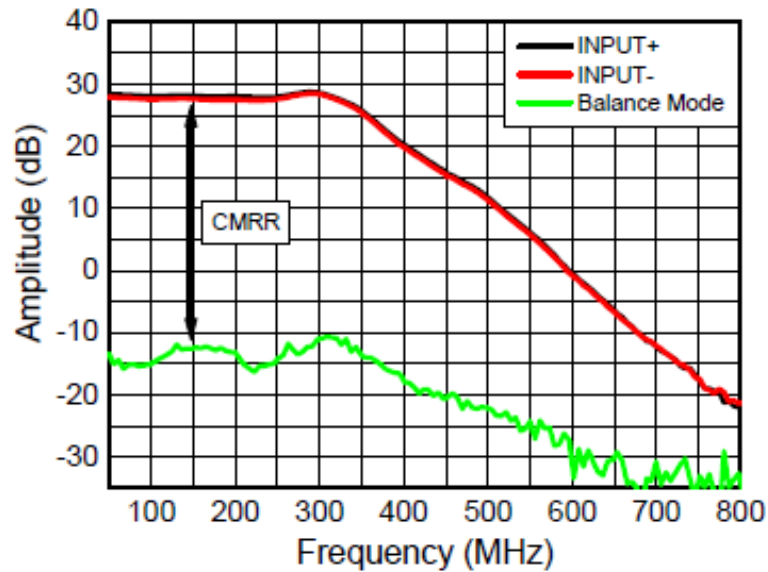


Figure 2.8 Frequency response of PDB130C

The Thorlabs PDB 130 balanced detector amplifier has a transimpedance gain of 10×10^3 V/A for high impedance loads and 5×10^3 V/A for 50Ω loads. The wavelength responsivity of 820nm wavelength is 10V/mW. If the differential power of the two optical inputs is greater than $700\mu\text{W}$, the amplifier will reach saturation. The bandwidth of the module PDB130A is from DC to 350MHz.

The 50-50 coupler can be modeled as a 50-50 non-polarization beam splitter. Both the beam $E_s \cos(\omega_r t + \phi_r)$ from signal arm and the beam $E_r \sin(\omega_r t + \phi_r)$ from reference arm will pass half and reflect half of the total power.

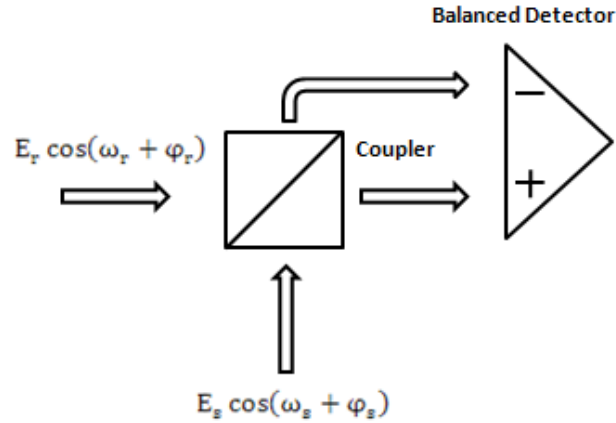


Figure 2.9 Principal of 50-50 coupler

The electric field at positive input of the differential detector is given by

$$E_+ = \frac{\sqrt{2}}{2} E_s \cos(\omega_s t + \varphi_s) + \frac{\sqrt{2}}{2} E_r \sin(\omega_r t + \varphi_r)$$

The electric field at negative input of the differential detector is given by

$$E_- = \frac{\sqrt{2}}{2} E_s \sin(\omega_s t + \varphi_s) + \frac{\sqrt{2}}{2} E_r \cos(\omega_r t + \varphi_r)$$

The quadrature phase relationships for the electric field on the two output ports represents the inherent phase shift caused by the beam splitter. Because the power detector is a square law detector, the voltage output is proportional to the square of the electrical field of the input signal,

For the positive voltage output

$$V_{01} = \frac{1}{2} G_\lambda \{ E_s^2 \cos^2(\omega_s t + \varphi_s) + E_r^2 \sin^2(\omega_r t + \varphi_r) + E_s E_r \sin[(\omega_s + \omega_r)t + (\varphi_s + \varphi_r)] \\ + E_s E_r \sin[(\omega_r - \omega_s)t + (\varphi_r - \varphi_s)] \}$$

For the negative voltage output

$$V_{02} = \frac{1}{2} G_{\lambda} \{ E_s^2 \sin^2(\omega_s t + \varphi_s) + E_r^2 \cos^2(\omega_r t + \varphi_r) + E_s E_r \sin[(\omega_s + \omega_r)t + (\varphi_s + \varphi_r)] \\ - E_s E_r \sin[(\omega_r - \omega_s)t + (\varphi_r - \varphi_s)] \}$$

Due to the ultra-high optical frequency of both ω_r and ω_s , only $\omega_r - \omega_s$ is a detectable frequency, thus only the term $E_s E_r \sin[(\omega_r - \omega_s)t + (\varphi_r - \varphi_s)]$ will be kept. The rest terms are only shown as dc value. The final output from the balanced detector is proportional to

$$G_{\lambda} E_s E_r \sin[(\omega_r - \omega_s)t + (\varphi_r - \varphi_s)]$$

With a constant reference signal and demodulation signal, the information contained in E_s can be easily extracted.

Electrical Domain

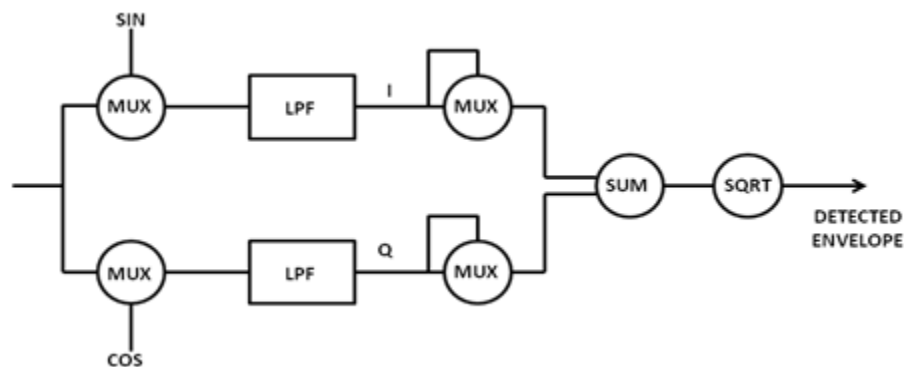


Figure 2.10 Diagram of electrical domain

As discussed earlier, the output of the balanced detector contains the information of the amplitude of the detected signal and it is centered at 40MHz which allows a 20 MHz bandwidth of the input signal. Given proper demodulation electronics, the

amplitude can be extracted. In another word, the demodulation circuit is an envelope detector.

The detected signal can be described as

$$S(t) = A(t)\sin(\omega t + \varphi(t))$$

where ω is the carrier frequency and φ is the phase relative to the reference signal. Two quadrature phase signals are

$$Q_1(t) = \cos(\omega t) \text{ and } Q_2(t) = \sin(\omega t)$$

In order to detect the $A(t)$, an approach called quadrature demodulation is utilized.

In the first path, $S_1 = S(t) * Q_1(t) = A\sin(\omega t + \varphi) * \cos(\omega t) = \frac{1}{2}A\sin(2\omega t + \varphi) + \frac{1}{2}A\sin\varphi$

As we can see, the dc value is dependent on the phase φ . In the second path,

$$S_2 = S(t) * Q_2(t) = A\sin(\omega t + \varphi) * \sin(\omega t) = -\frac{1}{2}A\sin(2\omega t + \varphi) + \frac{1}{2}A\sin\varphi$$

Both paths have a high frequency component and a DC component

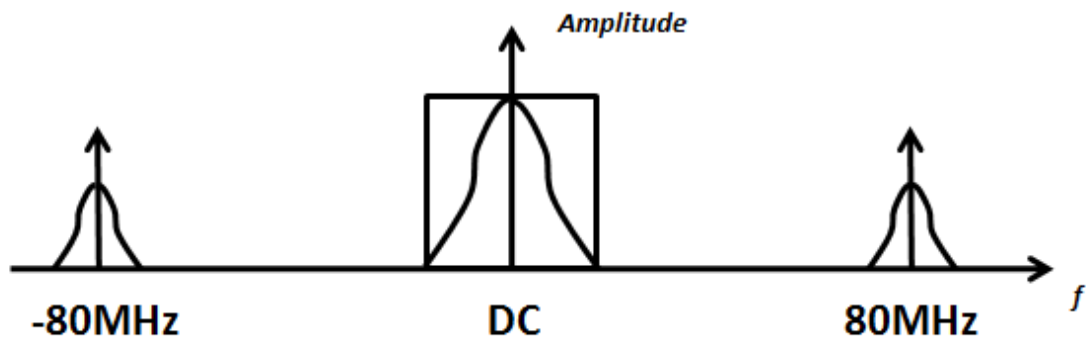


Figure 2.11 Low pass filter reserves the baseband signal

When the signal passes through a low pass filter, it only keeps the baseband component, thus, after the low pass filter

In the first path

$$S_1 = \frac{1}{2}A\sin\varphi \quad S_2 = \frac{1}{2}A\cos\varphi$$

Then, both paths go through a self multiplier

$$S_1 = \frac{1}{2}A\sin\varphi * \frac{1}{2}A\sin\varphi = \frac{A^2}{4}\sin^2\varphi$$

$$S_2 = \frac{1}{2}A\cos\varphi * \frac{1}{2}A\cos\varphi = \frac{A^2}{4}\cos^2\varphi$$

Add these two signals together,

$$S_1 + S_2 = \frac{A^2}{4}\sin^2\varphi + \frac{A^2}{4}\cos^2\varphi = \frac{A^2}{4}$$

After a root of square circuitry, the amplitude of the input signal will be acquired, obviously, the output amplitude is actually half of the real amplitude. Figure 2.12 shows the demodulation of ramp, square and sine modulated signal using the circuitry.

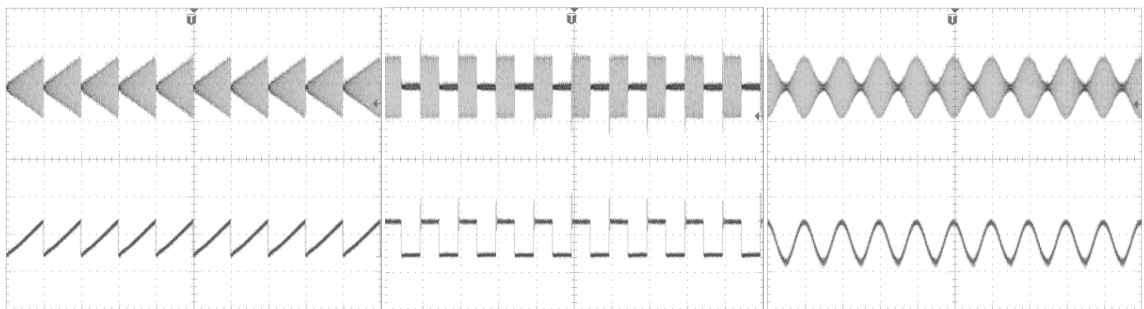


Figure 2.12 Ramp, square and sine modulated signal and demodulated signal

For the demodulation circuitry, quadrature phase reference signals are needed. In addition, the signals should have a fixed phase relationship with the input signal, which means they should be synchronized with the RF signal of the acoustical-optical modulator. Therefore, a power splitter is used to generate the required quadratic signal. The AOM RF driving signal is connected to the sum port, and quadrature phase signals can be achieved at port 1 and port2. Refer to figure 2.13 for a diagram of power splitter.

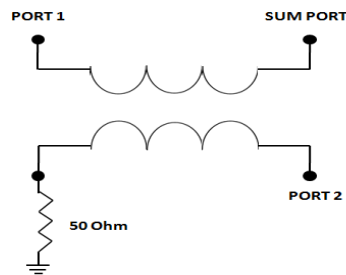


Figure 2.13 Diagram of power splitter

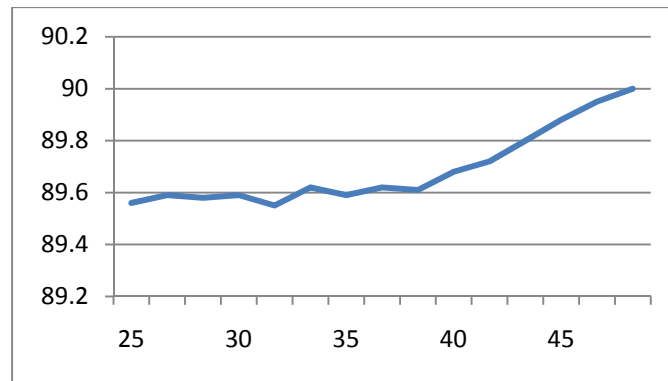


Figure 2.14 Typical performance for phase unbalance

ZMSCQ-2-50 model from Mini-Circuit is the one we use in our system. It features low insertion loss, typically 0.3 dB and high isolation, 27 dB typically. The operating frequency range is from 25MHz to 50MHz. Figure 2.14 shows the typical

phase unbalance is less than 0.4° . The disadvantages are that the power splitter has a maximum 3 degrees phase unbalance and 1.5 dB amplitude unbalance, which can be easily balanced by an additional attenuation and phase shifter.

Image Formation

Image formation is accomplished with an analog amplifier and image acquisition (IMAQ) from National Instruments. Due to the response from the skin sometimes does not necessarily meets the input level of the image IMAQ card, an analog amplifier was designed to interface the demodulation circuitry and the IMAQ card. The amplifier has two channels which are linear amplification and logarithm amplification. The latter channel is mostly used when response is extremely little due to its stronger amplification for small signals. Beyond the input voltage level, the IMAQ also needs two synchronization signals: vertical synchronization (Vsync) and horizontal synchronization (Hsync). These two signals can be acquired from the driver of scanning MEMS and then get buffered in the analog amplifier, finally sent to the IMAQ card.

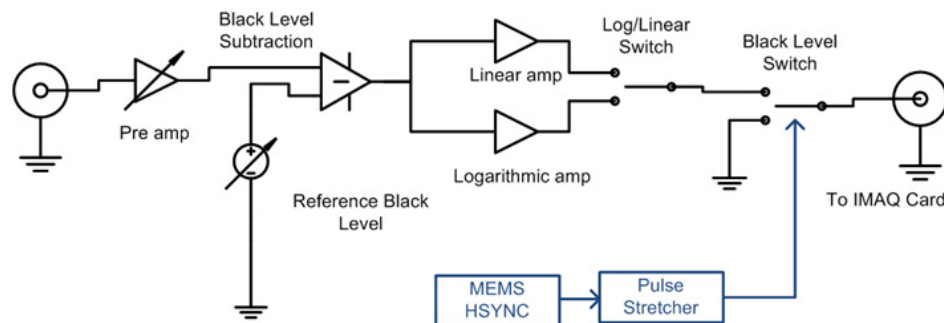


Figure 2.15 The amplifier design [9]

Figure 2.15 shows the amplifier design consists of a preamplifier, black level adjustment and logarithmic or linear amplification.

In order to construct image on the computer interface, we need to introduce the synchronization signal to the frame grabber. The synchronization signal, HSync and VSync are generated from the MEMS controller (PicoP™ Evaluation Kit). The PEK has two video interfaces:

- 1) Standard analog RGB VGA interface (VESA standard) or,
- 2) Microvision digital 24-bit RGB interface.

The standard analog RGB VGA interface is easily used in the projector mode, the MEMS can be turned on and turn off very quickly, but it does not provide the synchronization signals. The Microvision digital 24-bit RGB interface has 50 pins, and includes the necessary Hsync and Vsync signals. The required pins are listed below.

Table 2.1 MEMS driver interface

32	HSYNC	HSYNC_OUT synchronized to MEMS	Output	0 to 1.8-3.3V
33	GND	-	-	-
37	PB	Power button (pulled up to external power)	Input	0-5V
38	GND	-	-	-
39	VSYNC	VSYNC_OUT synchronized to MEMS	Output	0 to 1.8-3.3V
40	GND	-	-	-
42	POWER	Power supply	Input	5V±0.5V
43	GND	-	-	-

A custom board is built to interface the traces list above, and then the Hsync and Vsync can be used to form the image

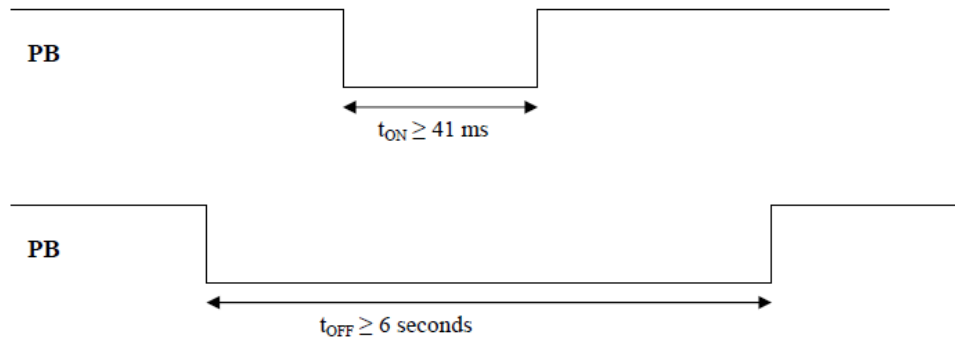


Figure 2.16 PEK turns on/off sequence

According to the PEK turn on/off sequence, the PB signal has to be pulled to the logic level “0” and remain at least 41ms in order to turn the MEMS on. To turn the MEMS off, the PB has to be pulled to the logic level “0” and remains at least 6 seconds. The PB is pulled to logic level “1” by an internal pull-up resistor voltage at the rest of the time. A pushbutton on/off switch was built to turn the MEMS scanner on and off.

Finally the imaging is acquired with the NI Measurement Studio which can capture snap images and display videos.

OPTICAL DESIGN

Several important elements are critical to acquire a confocal image and reject the out-of-focus light in the confocal microscope system. These elements consist of point illumination, point detection, and a scanning method [9]. As discussed in the first chapter, a pinhole is used as a spatial filter in the confocal microscope system to only accept the light from the focal plane. In the confocal system described in this paper a single mode fiber functions as the pinhole. Scanning is accomplished by a new MEMS two-dimensional scan mirror to scan the beam across the sample. This chapter will first detail the optical layout and design constraints for the confocal microscope. Later, theoretical performance measurements and Zemax optical simulation will be presented.

Optical Layout

For skin cell detection, a numerical aperture (NA) >0.7 is desirable and generally a field of view from 200 and 400 microns with a spatial resolution of one micron is sufficient for detection for skin cells. In order to achieve these requirements, the objective lens and the characteristics of the MEMS scanning mirror should be taken into account.

The MEMS scan mirror used in this system is manufactured by Microvision Inc. Figure 3.1 shows photos of the mirror and its housings. A magnetic housing surrounds the mirror which is used for the actuation scheme. The mirror is mounted to hinges, one of which pivots in horizontal direction and the other pivots in the vertical direction. It scans at 18 KHz in the horizontal direction with a small angle and 60Hz at the vertical direction with a big angle. The scanning scheme produces a rectangular pattern.

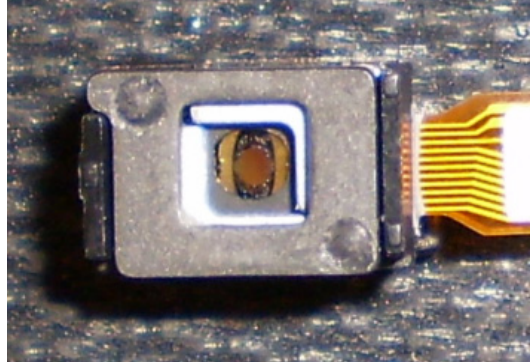


Figure 3.1 Photos of the MEMS scanning mirror

Table 3.1 Properties of the MEMS scanning mirror

Parameter	Value
Mirror clear aperture	1mm Diameter
Horizontal scan angle	11.6°-12.6°
Vertical scan angle	6.5°-6.9°
Horizontal scan frequency	18KHz
Vertical scan frequency	60Hz

At the beginning, a beam profile of the laser source should be gathered. Figure 3.2 shows the plot of the measured beam profile. The beam width is 222pixels, in which 1 pixel corresponds to 14.8 μm . Thus we can make a conclusion that the beam width is roughly 3.3mm.

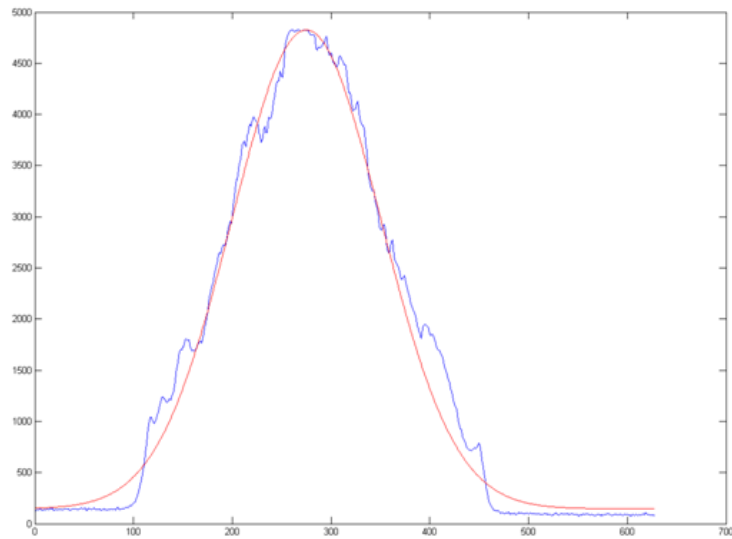


Figure 3.2 Beam profile

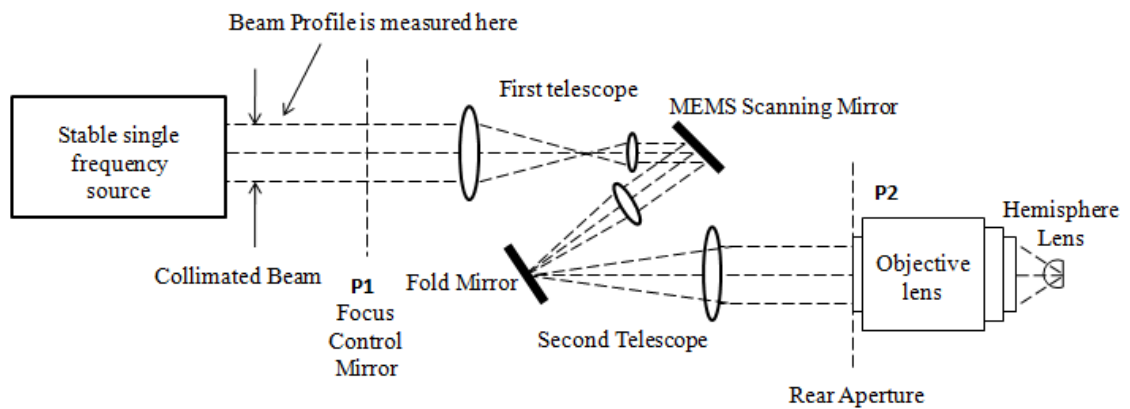


Figure 3.3 Block diagram of instrument subsystems

In the Figure 3.3, it shows how the beam size is adjusted by the telescope lens. The collimated beam has a 3.3mm diameter which is larger than the size of the MEMS scanning mirror. Therefore, a telescope lens which decreases the size from 3.3mm to 1mm is necessary to preserve all the optical power. The first telescope is also used to

relay the image from plane P1 (Figure 3.3) onto the MEMS scan mirror. P1 is therefore a conjugate plane to the MEMS scanner where the focus control mirror will be placed in the future.

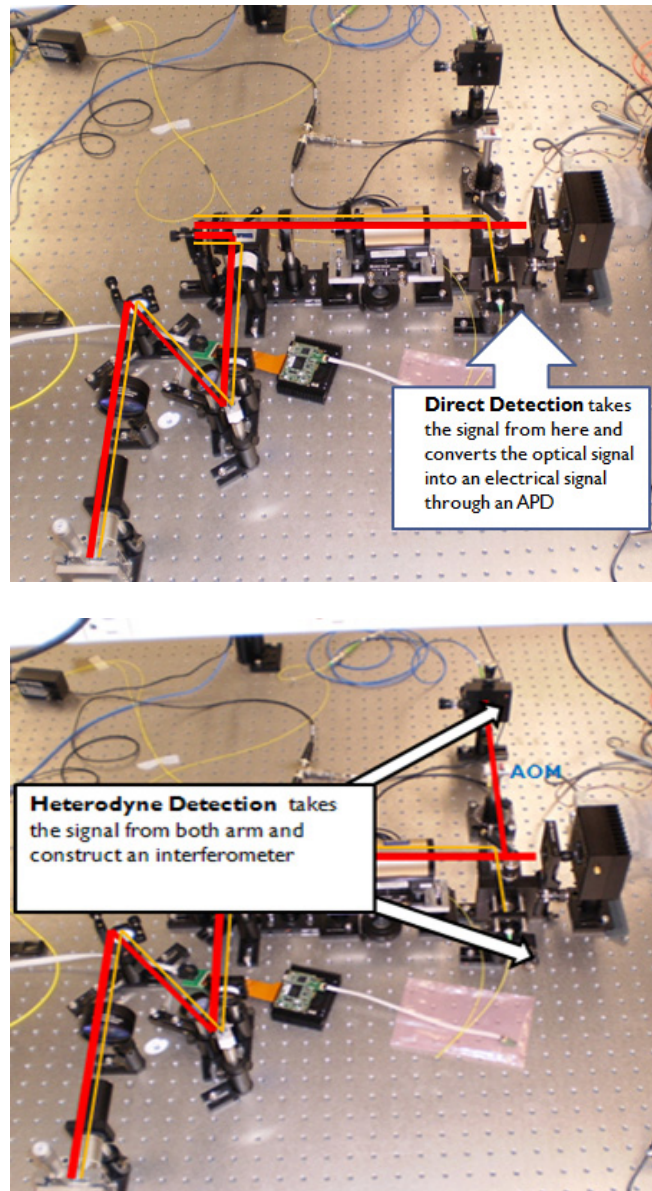


Figure 3.4 Optical setups of direct detection and heterodyne detection

To ensure the magnification of the image remains constant when the focus of the object is changed, the system was designed to be telecentric, which means that the chief ray is always parallel to the optical axis in the object space, and the exit pupil is located at infinity. There are two major reasons for including the second telescope lens, one is to make an image of the MEMS scanning mirror in the back focal plane (P2) of the objective lens. This guarantees the uniform illumination, which provides constant illumination and NA across the field of view, and results in telecentric operation. The other reason is that the rear aperture of potential objective lens is larger than 1mm. In order to get a large enough NA, the beam size should be increased to the same size as the rear aperture. In this system, an objective lens manufactured by Leica is mainly used. This objective lens has 100x magnification and 3mm exit pupil diameter. A telescope lens which can expand the beam size from 1mm to 3mm is needed.

Zemax Simulation

As discussed above, there are two optical relays and an objective lens in the microscope system. Due to the fact that the objective lens is a commercial microscope lens, we assume it is diffraction limited. Only the two telescopes are simulated in Zemax.

First Telescope

Based on the measurement, the beam size is 3.3 mm. For the purpose of fully filling the MEMS scanning mirror, the beam size should be minimized to 1mm. Thus a telescope which has a 3.3:1 ratio is built. The positioning of these lenses is critical for both the beam shrink and imaging the MEMS focus control mirror on the MEMS

scanning mirror and eventually the back focal plane of the objective, so Zemax was used to find the optimal lens location.

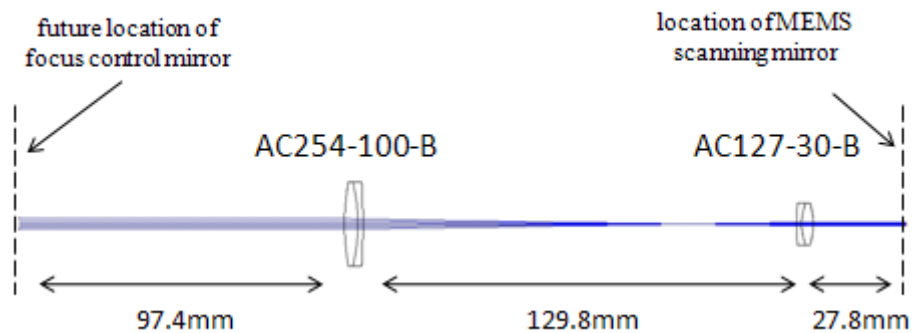


Figure 3.5 Zemax layout for telescope lens simulation

The telescope lenses we chose are AC 254-100-B and AC 25-30-B from Thorlabs Inc., these two lenses almost has the 3.3 ratio that we need to shrink the beam into 1mm diameter. There are three parameters we can adjust, the space between the lenses, the space between the MEMS focus control mirror and the first lens and the space between the MEMS scanning mirror and the second lens. With the initial 3.3mm entrance pupil diameter, our design goal is to get a 1mm diameter collimated beam at the exit pupil. For optimization, the targets include desired beam size and a collimated output beam. The optimal location is found in Figure 3.5.

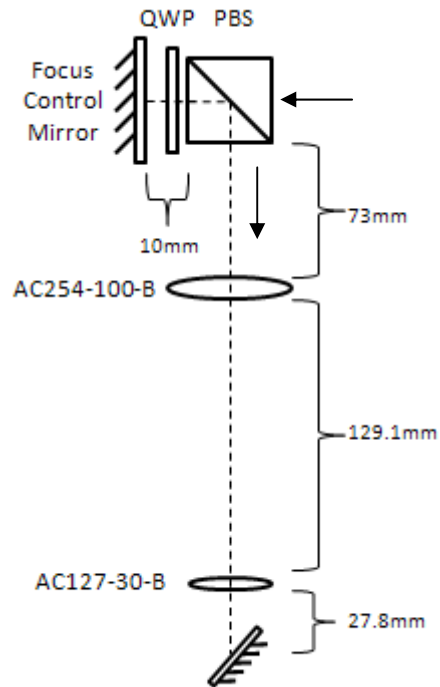


Figure 3.6 Optical layout for the first telescope lens

Considering the size of the polarization beam splitter and its index of refraction, we can find the distance in air between the focus control mirror and first lens is 83m. Due to the width of the quarter wave plate, we ignore its effect in enlarging the optical path. This distance can be adjusted as necessary. In this setup, we choose the value as it shows in Figure 3.6.

Second Telescope

The next step is to design the second telescope. An important parameter needed to build an accurate system in Zemax is the maximum scan angle of the MEMS mirror. This dictates what field angles will need to be modeled as well as the size and focal

length of the first lens in the telescope. By running the MEMS mirror with a laser beam incident on it the full angle of the optical scan was measured to be 26° . So, the maximum field angle for the Zemax model will need to be 13° , half the full angle. The necessary diameter lens with respect to focal length can be found as:

$$\tan(13^\circ) = \frac{D}{2f} \text{ or } \frac{D}{2f} \geq 0.23 \quad (3.1)$$

So, we need the first lens to have a diameter greater than approximately half its focal length.

To calculate the beam expansion needed from the telescope the diameter of the exit pupil of the microscope objective must be known. A Leica 100x 0.75 NA objective lens is used for all experiments and for this simulation. We use the equation below to calculate the exit pupil diameter.

$$f = \frac{\text{Tube length}}{\text{Magnification}} = \frac{200\text{mm}}{100} = 2\text{mm} \quad (3.2)$$

$$\text{exit pupil} = 2 \cdot NA \cdot f = 3\text{mm} \quad (3.3)$$

From the calculation we can find the exit pupil diameter is 3 mm and the input beam is 1 mm, therefore an approximate 3x telescope is needed.

The next procedure is to find a lens pair which has a ratio of 3 for the focal length. Two Thorlabs lenses were chosen to be used for the telescope: a 50mm 1" achromat (AC254-50-B) and a 150mm 2" achromat (AC508-150-B), both of which are AR coated for the NIR spectrum which match the laser source we use. Since both the input and output of the telescope will be collimated light, we can investigate which orientation will offer more consistent beam width for both on-axis and off-axis rays. But no matter which

configuration we use, the ratio of D/f is 0.5 for the first lens, which meets the constraints in (1).

To begin with, the two lenses were placed in a 1mm diameter zero degree field. Since the focal lengths of these two lenses are 50mm and 150mm, we put 200mm for the space between these two lenses as a starting point. Optimization for this spacing is to get a required 3mm collimated output beam. After finding the optimal spacing to be 194.43 mm, then a 13° field angle ray is added. The target of the optimization is to make the chief ray of the off-axis beam parallel with optical axis. This helps the system get a constant illumination and NA across the field of view. The location where both on-axis ray and off-axis ray intersect is back focal plane of the objective lens.

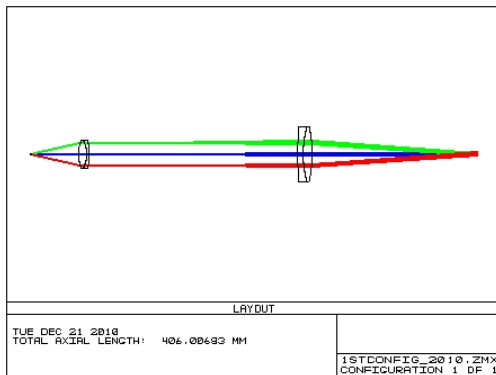


Figure 3.7 Optimization for beam width

Two different configurations are simulated, as shown in Figure 3.8. In the second configuration the directions of both lenses are reversed to investigate both the on-axis and off-axis performance. As we can see from the Figure 3.9 and Figure 3.10 as well as Table 3.2, although the second configuration has more aberration at the image plane for on-axis rays, it offers much better image performance at the image plane for off-axis rays. In

addition, the beam diameters are almost the same for the second configuration, which is superior to its counterpart of the first configuration. Moreover, the field curvature (FCUR) is much less in the second configuration compared with the first configuration at the image plane. We therefore choose the second configuration for the optical system. Following simulation will use it as a starting point.

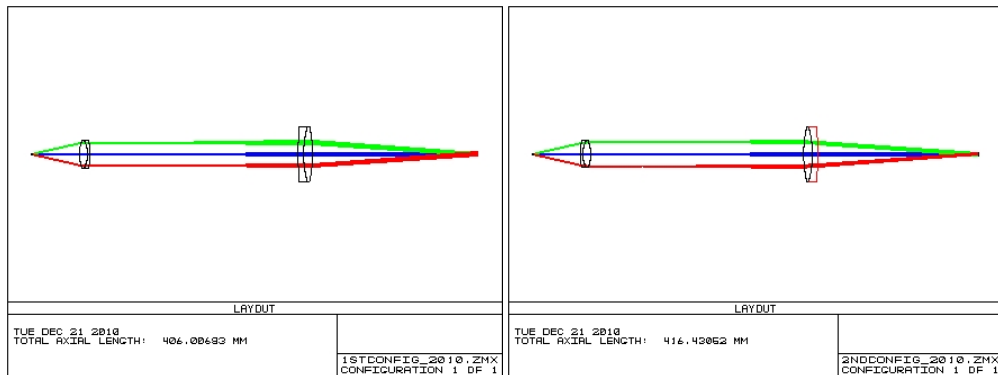


Figure 3.8 1st and 2nd configuration for telescope lens design

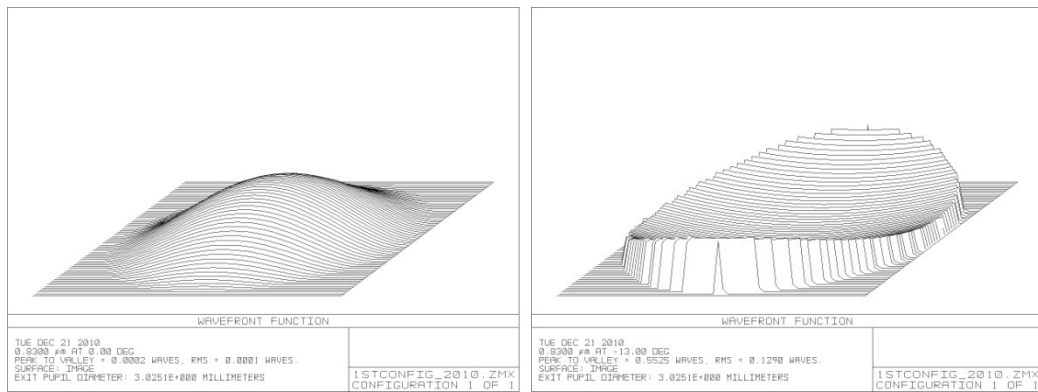


Figure 3.9 1st configuration and wavefront map for on-axis and off-axis ray

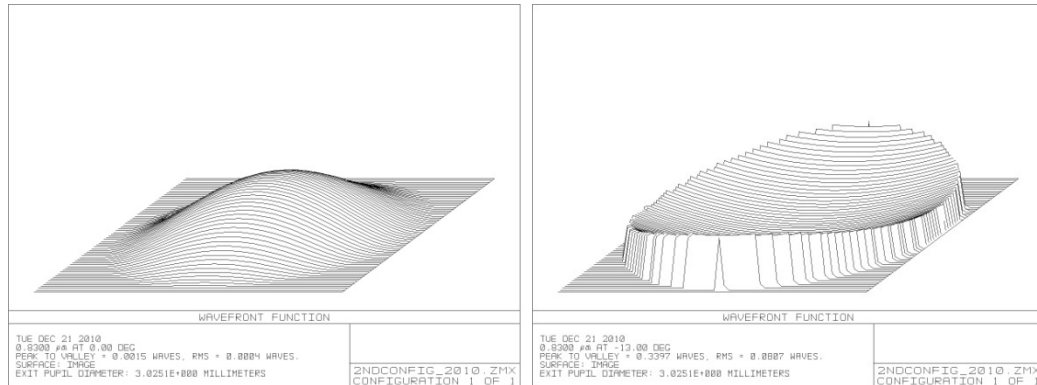


Figure 3.10 2nd configuration and wavefront map for on-axis and off-axis ray

Table 3.2 Comparison of 1st and 2nd configuration

	Peak to valley (waves)	RMS (waves)	Diameter of beam width (mm)	Field Curvature
1 st configuration 0°	0.0002	0.0001	2.97	0.014
1 st configuration 13°	0.5505	0.1290	3.67	
2 nd configuration 0°	0.0015	0.0004	2.94	0.0052
2 nd configuration 13°	0.3397	0.0807	2.96	

Objective Lens

The paraxial lens is used to simulate the ideal objective lens. Three lenses were used in the layout to achieve the beam expansion and NA described in the first order calculations. The first two lenses were 3 mm and 10.66 mm paraxial lenses and were placed so their focal points were in the same location to produce a beam expander. The last lens was a 4.7 mm paraxial lens placed with its first focal point at the right second focal point of the 10.66 mm lens for scanning.

Then a BK7 hemisphere lens is added to in the system. This BK7 lens is used to increase the objective NA and form the interface to the tissue for our microscope. A 6mm diameter hemisphere was chosen for this purpose because it is readily available in

our laboratory. The hemisphere was placed so rays out of the objective lens were focused to the center of the hemisphere. Knowing that the maximum field angle to the entire system is 13° , we can find the field angle to the objective lens is 4.3° to the paraxial lens system. Therefore we can use it as this field angle of the Zemax simulation for the optical system excluding the telescope, and the layout can be seen in Figure 3.11.

Paraxial objective lens is modeled with BK7 hemisphere front lens. It is important to note that the image surface was specified as 'seawater', which is an approximation of the index of refraction of skin. Finally, the inclusion of a variable thickness glass plate just before the hemisphere compensates for spherical aberration introduced when focusing into the tissue. In practice this plate can be provided using a microscope coverslip. Figure 3.12 shows the optical performance of the paraxial lens with the BK7 hemisphere.

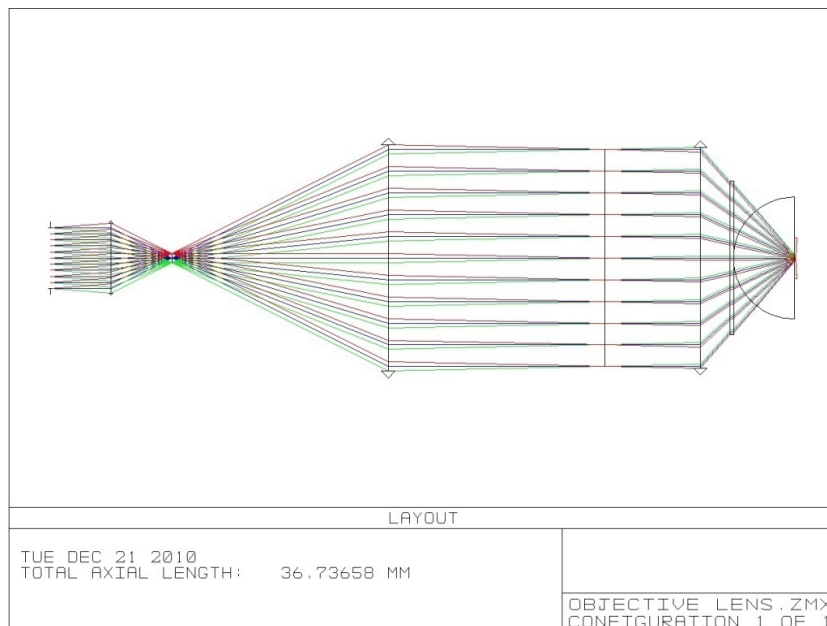


Figure 3.11 Paraxial objective lens

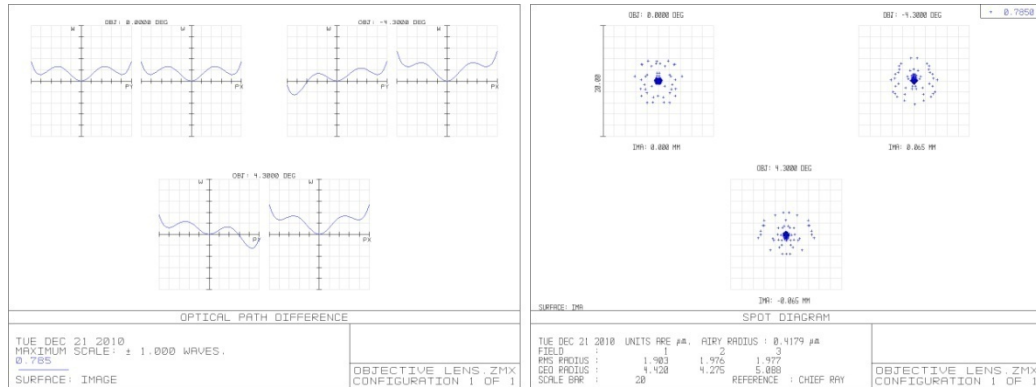


Figure 3.12 Optical performance for paraxial lens combined with hemisphere lens

Full System Layout

The last step in designing this confocal microscope was to combine the telescope with the objective and hemisphere lenses. The initial adjustment for the complete system was to place the left focal point of the first lens in the objective lens model at the point where the chief rays from the on-axis and 13° fields cross after the telescope. This is the pupil plane of the objective lens. This was first done manually by visually checking the intersecting point and changing the spacing to place the focal plane there. Figure 3.13 shows the layout of the complete system. To find the best focus for on axis and 13° fields the distance of the image plane from the flat surface of the hemisphere, the curvature of the image plane as well as a dummy surface were optimized with the default RMS spot radius merit functions.

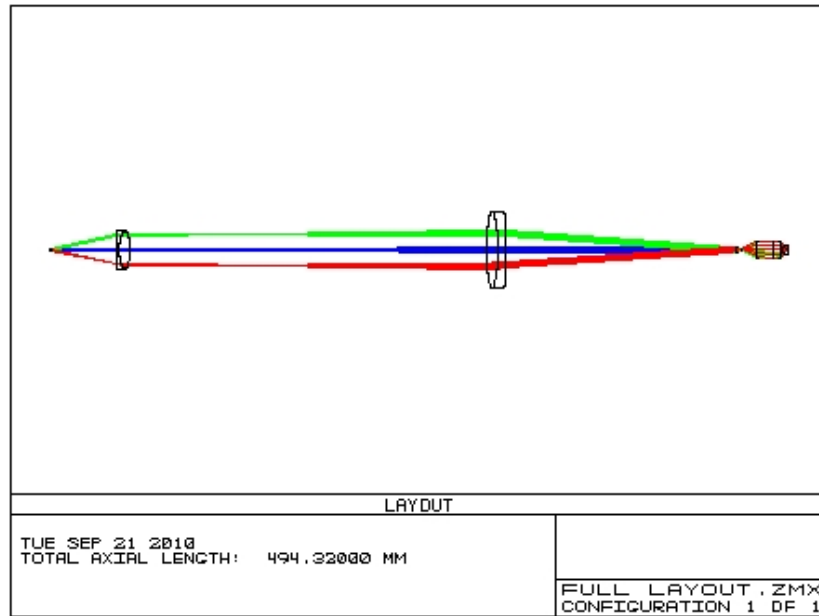


Figure 3.13 Layout of the complete system

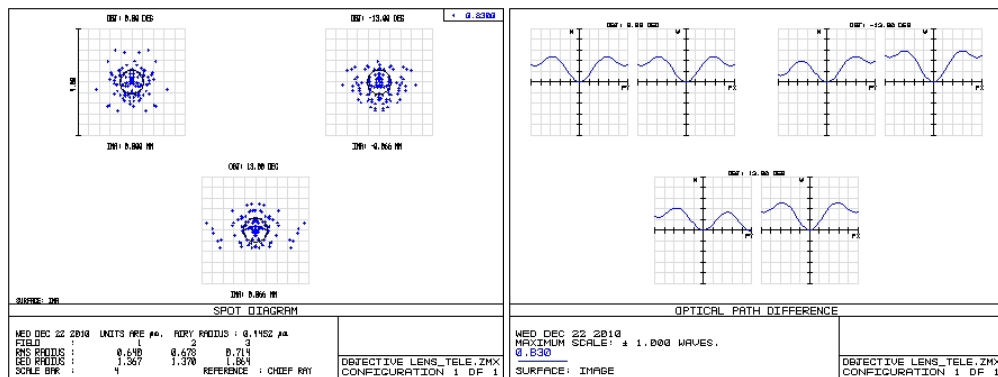


Figure 3.14 Spot diagram for the final design

The spot diagram for the final design is shown in Figure 3.14. For the aberration COMA is 0.232 and SPHA is dominant which is -0.63 for this system, the image quality for the off-axis ray is still within our specification.

NOISE ANALYSIS

The main reason that heterodyne detection is utilized in this system is its excellent noise performance compared to direct detection. Detectors are very critical component to instrumentation because they translate the characteristics of the physical world into electrical signals. We process and measure these signals and interpret them to be the optical reaction to the sample we are looking at.

Noise can be described as any type of undesired disturbance that obscures or interferes with a desired signal. In our system, the desired signal is the voltage level dependent on the optical reflectivity of the sample. Noise is important because the limit of resolution of a detector is often noise. The dynamic range of a system is determined by noise. The highest signal level that can be processed is limited by the characteristics of the circuit, but the smallest detectable level is set by noise. There are three major types of noise mechanisms, referred to as thermal noise, low-frequency ($1/f$) noise, and shot noise [11].

One of the virtues of heterodyne detection is that the signal is superimposed on a carrier frequency that is generally far removed spectrally from the potential noise radiated during the process of generating either the signal or the reference signal, narrow band clock noise, 60Hz noise and $1/f$ noise, thus making the spectral region near the carrier frequency relatively quiet [11]. Thus, the low-frequency ($1/f$) and most narrow-band interference noise are minimized.

The primary remaining source of noise is photon shot noise from the nominally constant level of the reference signal on the optical detector. Because the shot noise is

proportional to the amplitude of the reference signal electric field, and the heterodyne mixed signal is also proportional to the reference signal electric field, the ratio of the shot noise to the mixed signal is independent with the amount of the reference signal. With proper detection, the shot noise can be made dominant over the thermal noise and therefore sets the ultimate detection limit of the system. In practice, thermal noise at the detector may still be the dominant noise source.

Direct Detection

Before introducing the noise analysis of heterodyne detection, the analysis of direct direction is presented. The analysis is based on the C5460 avalanche photodiode (APD) module from Hamamatsu:

Table 4.1 Specification of C5460 module from Hamamatsu

Parameter	C5460
Photo sensitivity G_λ (V/W)	1.5×10^6
Power supply (V)	12
Photo sensitivity (A/W)	0.5
NEP ($\text{pW}/\sqrt{\text{Hz}}$)	0.2
Bandwidth	DC-10MHz

Dynamic Range Analysis for Direct Detection

We make an assumption that the signal bandwidth is 10M Hz, the practical video bandwidth of the system. Based on the definition of noise equivalent power we can find the minimum power the C5460 module can detect, limited by the thermal noise.

Minimum Detection Power

$$\begin{aligned}
 &= \text{NEP} \times \sqrt{\text{Bandwidth}} \\
 &= 0.2\text{pW}/\sqrt{\text{Hz}} \times \sqrt{10 \times 10^6} = 0.2 \times 10^{-12} \times 3.1 \times 10^3 = 0.62\text{nW rms}
 \end{aligned}$$

The maximum output signal is 10V

Maximum Detection Power

$$\begin{aligned}
 &= \frac{V_{\text{max}}}{G_{\lambda}} \\
 &= \frac{10\text{V}}{1.5 \times 10^6 \text{V/W}} = 6.7\mu\text{W}
 \end{aligned}$$

Dynamic Range

$$\begin{aligned}
 &= 10\log_{10} \left(\frac{\text{Maximum Detected Power}}{\text{Minimum Detected Power}} \right) \\
 &= \left(\frac{6.7\mu\text{W}}{0.62\text{nW}} \right) = 40.33\text{dB}
 \end{aligned}$$

The C5460 module has approximately 40dB dynamic range. In general, the output voltage level is proportional to the detected power which means they have a linear relationship.

Heterodyne Detection

For this application, a balanced detector is used to detect the interference sinusoid waveform. Based on the requirement for wavelength and bandwidth, we choose module PDB130C from Thorlabs.

Table 4.2 Specification of PDB 130C module from Thorlabs

Detector Material/Type	Si/PIN
Wavelength Range	320nm-1000nm
Typical Max. Responsibility	0.5A/W (S_λ)
Bandwidth	DC-350MHz
Conversion Gain RF-Output	5×10^3 V/W (G_λ)
CW Saturation Power	700 μ W @820 nm
Max. Input Power	20 mW
Minimum NEP (DC-100MHz)	14.7 pW/ $\sqrt{\text{Hz}}$ (differential)

Dynamic Range Analysis for Heterodyne Detection

At one detector has amplitude U_1 , where the electric field,

$$U_1 = (U_s + U_r + U_{ns} + U_{nr}) \frac{1}{\sqrt{2}}$$

U_s is the signal reflected back from the sample, U_r is the reference signal, U_{ns} and U_{nr} are the shot noise from U_s and U_r , respectively. The power is found as

$$P_1 \propto \langle |U_1|^2 \rangle$$

Therefore,

$$P_1 \propto \frac{1}{2} \langle U_s U_s + U_s U_r + U_s U_{ns} + U_s U_{nr} + U_r U_s + U_r U_r + U_r U_{ns} + U_r U_{nr} + U_{ns} U_s + U_{ns} U_r + U_{ns} U_{ns} + U_{ns} U_{nr} + U_{nr} U_s + U_{nr} U_r + U_{nr} U_{ns} + U_{nr} U_{nr} \rangle$$

After the uncorrelated terms are removed because the average value is zero, the result is

$$\frac{1}{2}(U_s U_s + 2(U_s U_r) + U_r U_r + U_{ns} U_{ns} + U_{nr} U_{nr})$$

Since $U_s \ll U_r$ and $U_{ns} \ll U_{nr}$ because the reference power is assumed much larger than the signal beam power

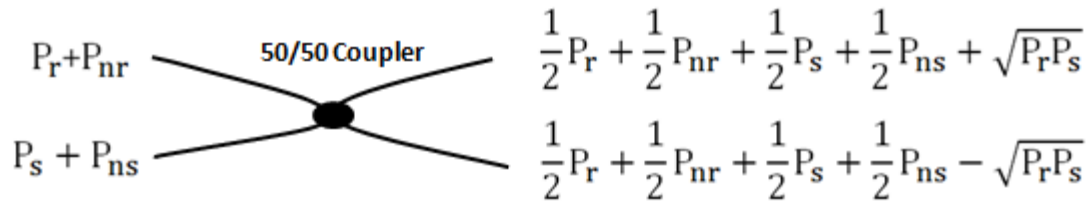


Figure 4.1 The power distribution of 50/50 coupler

For one detector, the input power is therefore

$$P_1 = \left(\frac{1}{2}P_r + \sqrt{P_r} \sqrt{P_s} + \frac{1}{2}P_{nr}\right)$$

On the other detector, due to phase shifts occurring at the beam splitter

$$P_2 = \left(\frac{1}{2}P_r - \sqrt{P_r} \sqrt{P_s} + \frac{1}{2}P_{nr}\right)$$

When the signal from detector 1 is subtracted from the detector 2, the voltage output of the balanced detector will be

$$P_{\text{diff}} = 2\sqrt{P_r} \sqrt{P_s} + KP_{nr} \quad \text{where } 0 \leq K \leq 1$$

It shows that the power to be detected does have a component from the shot noise of reference power. The effect of the shot noise was measured and can be ignored when compared with the thermal noise of the detection, which means the thermal noise from the amplifier becomes the dominant noise.

Since the balanced detector has a $700\mu\text{W}$ saturation power, for the maximum signal we can detect

$$2\sqrt{P_r P_{s\max}} = P_{\text{sat}}$$

$$P_{s\max} = \frac{P_{\text{sat}}^2}{4P_r}$$

For the minimum signal we can detect

$$2\sqrt{P_r P_{s\min}} = \text{NEP}$$

$$P_{s\min} = \frac{\text{NEP}^2}{4P_r}$$

According to the definition of dynamic range

$$\text{Dynamic Range} = 10\log \frac{P_{s\max}}{P_{s\min}} = 10\log \frac{P_{\text{sat}}^2}{\text{NEP}^2} = 78.6\text{dB}$$

Compared with analysis from direct detection, the dynamic range has been improved by almost 30dB which offers the possibility of deeper optical penetration into tissue for the microscope.

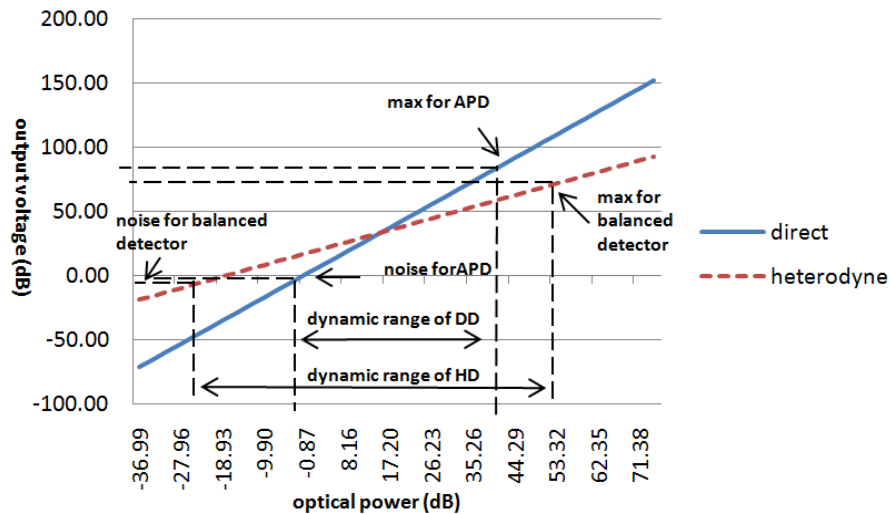


Figure 4.2 Dynamic range comparisons of direct detection and heterodyne detection

Figure 4.2 shows the theoretical comparison of direct detection and heterodyne detection. Both the detected optical power and output voltage are shown in a log scale. The direct detection has smaller dynamic range due to its larger minimum detectable power and smaller maximum detectable power. The heterodyne detection has smaller minimum detectable power and larger maximum detectable power mainly because in heterodyne detection the output voltage is proportional to the square root of the signal power which is shown in the graph that the slope of heterodyne detection trace is only half of its counterpart in the direct detection trace.

RESULTS

When the confocal microscope with heterodyne detection system is built, the primary goal is to evaluate the optical performance compared with theoretical estimations. To do this we measure the edge and axial response of the heterodyne system compared to the direct detection system. In addition, the noise performance should also be evaluated, to verify that the heterodyne system is indeed able to measure weaker signal than the direct detection system. Once the characterization of the system is achieved, we can start testing imaging capabilities in scattering samples including plant tissue and human skin.

Optical Performance

The first step is to assess edge response and axial response measurement which defines the optical performance. These two measurements can be used to describe the point spread function that describes the resolution of the confocal imaging system. Also, the edge response relates to the minimum resolvable feature size, which is critical to confocal image formation [9]. The approaches for acquiring the edge and axial response data will be presented separately. The measurements were made using the objective lens without the glass hemisphere, with the primary purpose to demonstrate the comparative performance when using direct detection and heterodyne detection.

Edge Response with Direct Detection using the APD

The imaging capability is often evaluated by a point spread function. The point spread function represents the response of the optical system to point source object. The point spread function is critical for the characterization of the lateral response. Due to the complexity for the direct measurement of the point spread function, a measured edge response is used to compare with the theoretical values. With direct detection, it can be shown that the confocal system response is given by [12]

$$I = |E_s|^2 \quad (5.1)$$

$$E_s = |p^2 * s|^2 \quad (5.2)$$

where $s=s(x, y)$ is the sample reflectivity and $p=p(x, y) = p(r)$ is the optical field in the sample plane. For the assumed case where the sample is a point reflector, therefore,

$$I = |p(r)|^4 \quad (5.3)$$

The point spread function resulting from a Gaussian beam input and with no aberration (the diffraction limited case) can be described as [13]

$$I(r) = \left| KA \int_0^1 e^{-\frac{A}{2}p'^2} J_0 \left(2\pi \frac{a_0}{f} rp' \right) p' dp' \right|^4 \quad (5.4)$$

where a_0 is the pupil radius at the aperture stop, f is the focal length of the objective. The A parameter is used to compare the pupil radius a_0 and the Gaussian beam radius ω . When the pupil radius and the Gaussian beam radius are the same, $A=2$. In our case, the pupil is little overfilled which gives us the A parameter =1.67.

$$A=2\left(\frac{a_0}{\omega}\right)^2 \quad (5.5)$$

Mathematically the edge response function (EDRF) is the integral of the line spread function; the line spread function (LSF) is the integral of the point spread function (PSF). As shown in Figure 5.1, for $A=1.67$ (our case) the theoretical edge response distance is $0.5\mu\text{m}$.

$$LSF(x) = \int_{-\infty}^{+\infty} PSF dy \quad (5.6)$$

$$EDRF(x) = \int_{-\infty}^x LSF dx \quad (5.7)$$

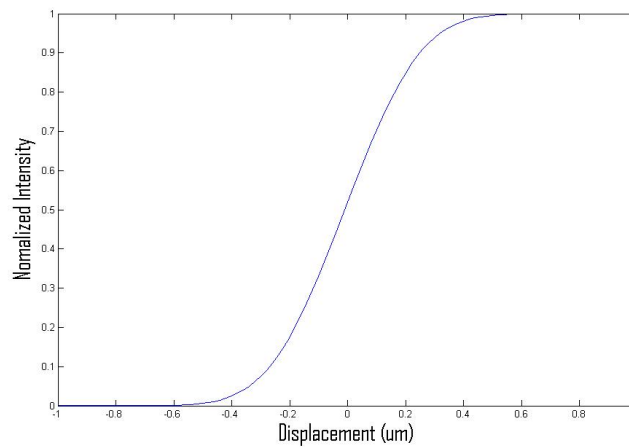


Figure 5.1 Normalized edge response of direct detection

The edge response for the CLSM is measured with shiny metallic area on a piece of silicon. This gives us a really sharp edge with a highly reflective surface. The metal layer thickness is less than 100nm, and the phase associated with the step height has been neglected. This silicon piece is placed on a three-dimensional translation stage and an image of the metallic area on the silicon is achieved. We can adjust the translation stage to target on a letter with a sharp edge like ‘E’ and ‘I’ which shows in Figure 5.2. The object should be perpendicular to the fast scan which scans horizontally. With the target

letter placed in the imaging area and at the best focus, we can see the APD output waveform on the oscilloscope. The voltage level exactly corresponds to the shiny area when the laser beam scans horizontally.

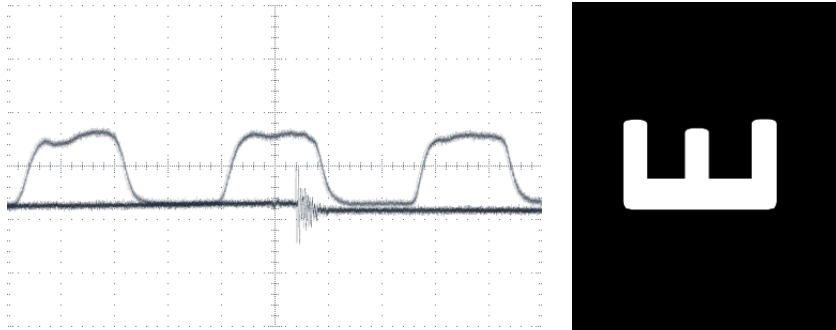


Figure 5.2 A letter 'E' on the object is used to represent an edge

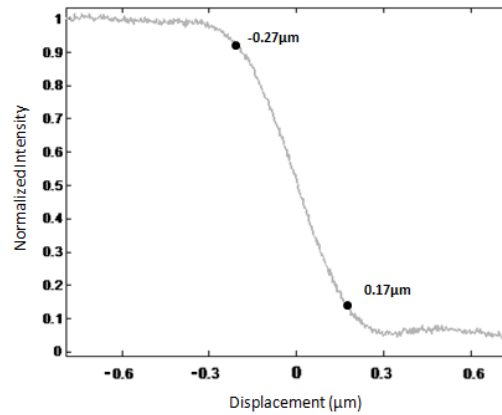


Figure 5.3 Calibrated oscilloscope trace

Then the measurement has to be calibrated with the known dimension of the structured reflector, which is done in Figure 5.3. We are looking for the distance from the 90% intensity to 10% intensity. The measured result is $0.54 \mu\text{m}$. The theoretical value calculated using Equation 5.6 is $0.49 \mu\text{m}$. We conclude that the microscope is operating near the diffraction limit.

Axial Response with Direct Detection Using the APD

The axial imaging properties of a confocal microscope using a single mode fiber as a detector are analyzed. In order to investigate the optical sectioning property of confocal microscopes it is instructive to consider the intensity recorded as a planar surface is scanned axially through the focal spot. This is known as the axial response. The intensity I varies with defocus parameter u according to equation 5.8[12].

$$I(u) = \frac{A^2}{A^2+u^2} (1 + e^{-2A} - 2e^{-A} \cos u) \quad (5.8)$$

where A is parameter used in equation 5.5. The defocus parameter u is given by

$$u = 2\pi \frac{z}{\lambda} NA^2 \quad (5.9)$$

This is the response for a conventional detection scheme where the measure signal is proportional to the optical intensity I . In our system, $NA=0.75$, $\lambda=830\text{nm}$ and z is the distance from the focus.

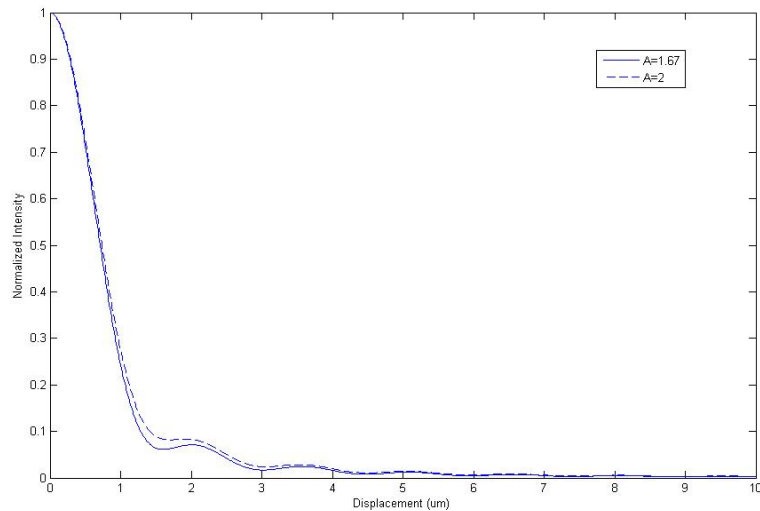


Figure 5.4 Normalized axial response curves

Figure 5.4 shows the normalized axial response curves with different A with $NA=0.75$. As we can see from Figure 5.4, the axial response with $A=2$ and $A=1.67$ is very close, which gives us an estimated $FWHM=1.2\mu m$. The axial response is measured by placing a mirror in front of the object lens with a piezo-actuator between a three-dimensional translation stage and the mirror. When we applied voltage to the piezo-actuator, it moves forward and backward with $10\mu m$ in total. Thus we can have a periodic signal waveform on the oscilloscope. With calibration, we can have a plot which shows normalized intensity is a function of displacement. The axial response measurement takes the displacement the system needs to move from 50% normalized intensity from one side to another. The full width half maximum of the response is measured in the time scale, which is $38.4ms$. To calibrate the result, a reference measurement is made, the translation stage is moved $2\mu m$ and a second measurement is made. The translation of a particular feature measured to be $57.2ms$. Then the axial response can be calibrated by the measured relationship between time scale and displacement. An axial width of $1.2\mu m$ FWHM is measured. Table 5.1 shows the theoretical and experiment values for the edge and axial response of the microscope with direct detection.

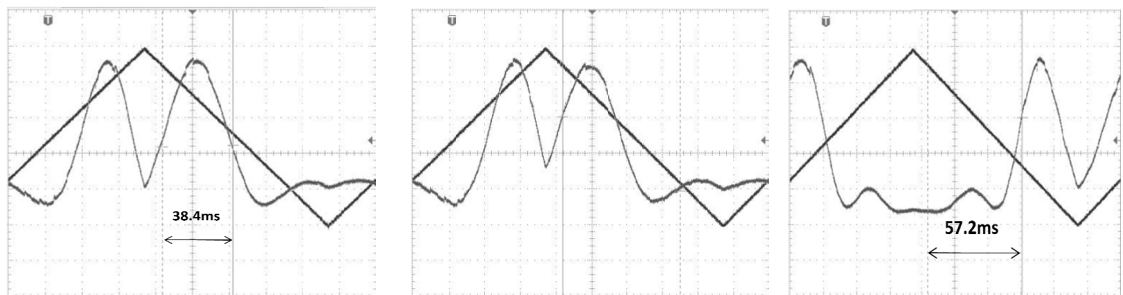


Figure 5.5 Measured result of axial response

Table 5.1 Theoretical and measured optical performance in direct detection

	Edge Response	Axial Response
Theoretical value	0.49 μm	1.2 μm
Measured Value	0.54 μm	1.2 μm

Edge Response with Heterodyne Detection

In the direct detection system the intensity of the light coupled into the detection fiber I is given by

$$S_D \propto I \propto |U|^2 \quad (5.10)$$

With direct detection the APD signal is proportional to intensity I . For heterodyne detection, the measured signal is proportional to \sqrt{I}

$$S_H \propto \sqrt{I} \propto |U|^2 \quad (5.11)$$

In our heterodyne system, with linear amplification the edge response

$$EDRF = \int_{-\infty}^x \int_{-\infty}^{+\infty} S_H dydx \quad (5.12)$$

with log amplification the edge response

$$EDRF = \log\left(\int_{-\infty}^x \int_{-\infty}^{+\infty} S_H dydx\right) \quad (5.13)$$

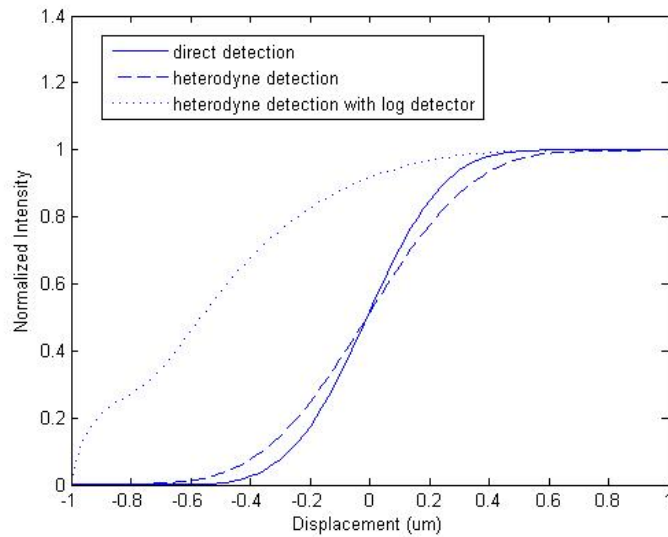


Figure 5.6 Normalized edge responses of direct detection, heterodyne detection and heterodyne detection with log detector.

Based on the different expressions of intensity, the theoretical edge response can be derived. Figure 5.6 shows the theoretical edge response of both direct detection and heterodyne detection. The theoretical edge response distance of heterodyne detection is $0.71\mu\text{m}$ with linear amplification and $1.19\mu\text{m}$ with log amplification.

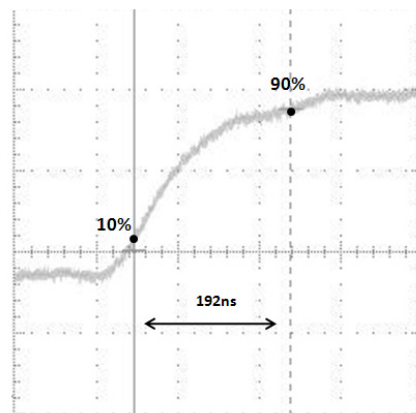


Figure 5.7 Measured edge response of heterodyne detection with log detector

The measurement from 10% of intensity to 90% of intensity on time scale is 192ns. Considering the time and distance relationship in edge response measurement, this corresponds to a $1.38\mu\text{m}$ edge response distance, which is slightly degraded compared to the theoretical expectation.

Axial Response with Heterodyne Detection

Similarly, the axial response in heterodyne detection can be derived from the intensity expression in heterodyne detection. Figure 5.10 shows the theoretical axial responses for different detection techniques.

$$S_D = \log\left(\sqrt{I(u) = \frac{A^2}{A^2+u^2} (1 + e^{-2A} - 2e^{-A} \cos u)}\right) \quad (5.14)$$

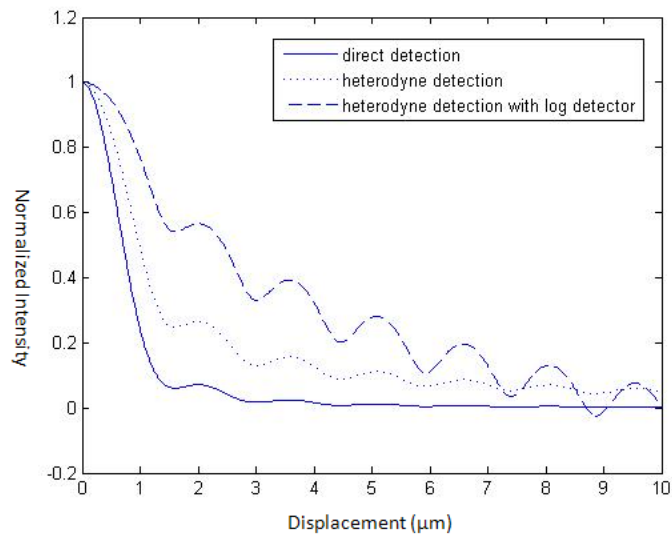


Figure 5.8 Theoretical axial responses of direction detection, heterodyne detection and heterodyne detection with log detector.

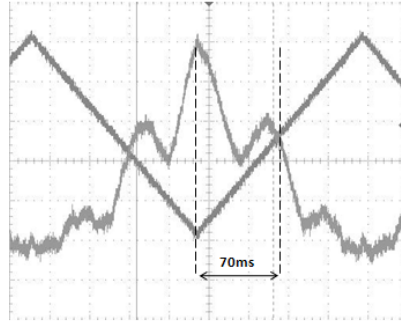


Figure 5.9 Measured axial response in heterodyne detection with log detector

The theoretical value of axial response of heterodyne detection is $1.6\mu\text{m}$ with linear amplification and $4.88\mu\text{m}$ with log amplification. The measurement of the axial response of heterodyne detection with a log detector has 140ms on time scale, which corresponds to a $5\mu\text{m}$ axial response distance. This matches quite closely our theoretical value, and indicates less cross-sectioning ability using heterodyne detection with a log detector. Table 5.2 shows the comparison of the theoretical and measured optical performance of the heterodyne detection system when using a log detector. Both measured results are close to the theoretical value. Only the log detector was used for our experimental validation of the edge and axial response of the microscope with heterodyne detection. But based on these results, we can reasonably conclude that the system is performing nearly at the diffraction limit, and the optical system imaging characteristics are well understood.

Table 5.2 Theoretical and measured optical performance in heterodyne detection

	Edge Response	Axial Response
Theoretical value	1.19 μm	4.88 μm
Measurement Value	1.38 μm	5 μm

Noise Performance

Dynamic Range

The dynamic range of direct detection and heterodyne detection can be proved by using different OD filters. Both direct detection and heterodyne detection are adjusted in order to have the maximum output voltage. OD filters are added to attenuate the signal until the output voltage is at the same level of the noise which is the minimum power the system can detect. Figure 5.10 shows the output voltage in terms of different OD values. It has a linear relationship and 40dB dynamic range. The minimum detectable power is 0.62nW, based on the photo-sensitivity the equivalent minimum detectable voltage is 0.93mV. At OD 4, the output signal is 1.1mV which is at the same level as the noise floor.

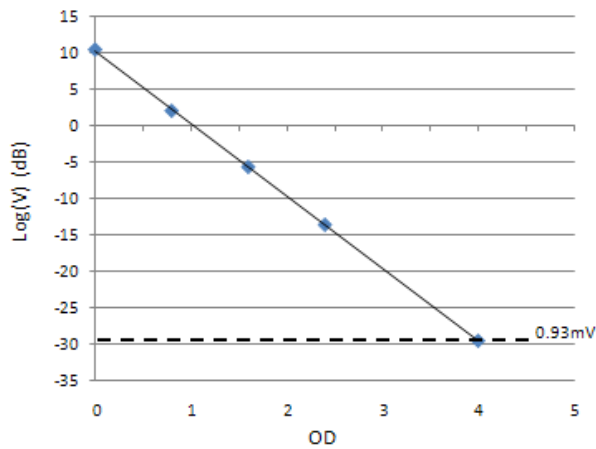


Figure 5.10 Measured dynamic range of direct detection

Figure 5.11 shows the characterization of heterodyne detection, using the same technique. In the log scale, the waveform is approximately a line as expected and the minimum signal can be detected when the OD value is 8. The theoretical minimum detectable power for heterodyne detection is 66nW , based on the photo-sensitivity the maximum detectable power is $660\mu\text{V}$. This gives an approximate 80 dB dynamic range for the measured optical power.

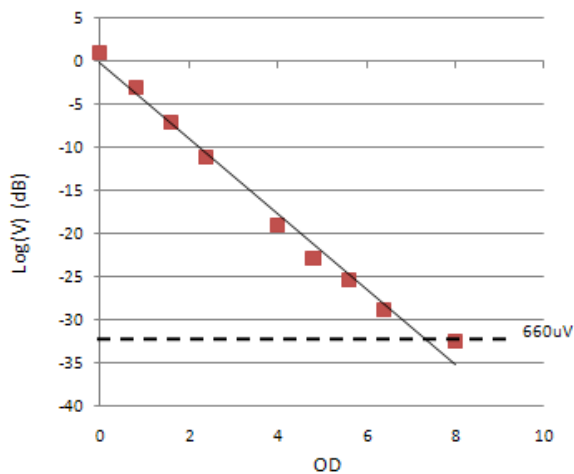


Figure 5.11 Measured dynamic range of heterodyne detection

Image

Figure 5.12 shows two example images of heterodyne detection imaging. The object of imaging is a piece of MEMS which has letters and a mirror on it. The vias on the mirror have a $30\mu\text{m}$ distance from each other, which indicates a $300\mu\text{m}$ diameter field of view. The overall field of view has a circular pattern instead of the rectangular scanning pattern is due to vignetting by the telescope lens. These two images are taken with the IQ demodulation circuitry. However, due to the unbalance of the quadrature phase signal and the inaccuracy of the local oscillation signal, the IQ demodulation circuitry does not offer satisfying imaging capability for small signals. In this case, an AD8703 log detector is used for tissue imaging. This same detector was used for the edge and axial response measurements presented earlier.

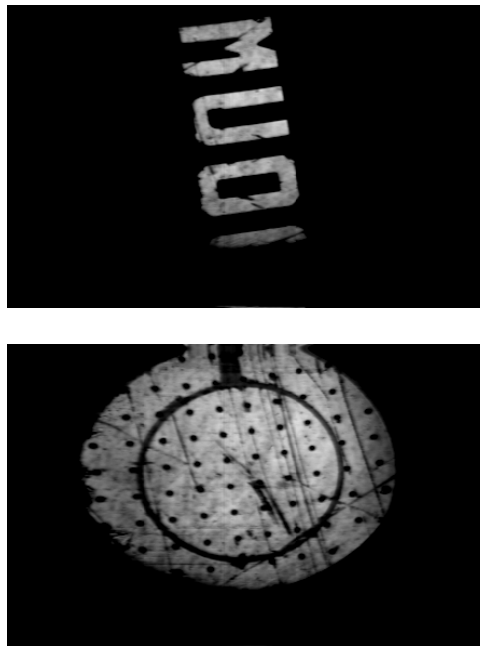


Figure 5.12 Example images of a MEMS mirror using heterodyne detection

Next step is to compare the imaging capability for both direct detection and heterodyne detection. In the both detection techniques, the imaging procedure starts from a saturated image which indicates the maximum voltage output. Filters with different OD values are applied to assess the ability to respond to small signals. We can verify the dynamic measurement here again by doing this experiment and we are able to see the difference between the two detection system in an imaging application. From figure 5.13 and 5.14 the theoretical result is proved that heterodyne detection has better performance in detecting small signals and thus gives the potential for deeper penetration in skin.



Figure 5.13 Images with OD 0, OD 1.6 and OD 4 in direct detection



Figure 5.14 Images with OD 0, OD 1.6, OD 4 and OD 8 in heterodyne detection

The detected power in both detection techniques is shown in Table 5.3. It can be seen that the heterodyne detection is able to image some features even with OD 8 attenuation,

while the direct detection is only able to image with OD 4 attenuation. The imaging experiment matches the result of dynamic range measurements.

Table 5.3 Detected power with certain OD

	OD 0	OD 1.6	OD 4	OD8
Direct Detection	10.4uW	0.27uW	0.83nW	N/A
Heterodyne Detection	0.58mW	14.5uW	58nW	5.8pW

Based on the attenuation of different OD filters and the gains of the detectors in both detection system, the detected power can be calculated. Table 5.3 shows the minimum power can be detected in both detection system with available OD filters.

When the images are taken on a plant sample, the advantages and disadvantages when imaging in scattering tissue can be found. All images of scattering material are made using log detection of the heterodyne signal. Figure 5.15, 5.16 and 5.17 shows that although the heterodyne detection has about 60 μ m deeper penetration than direct detection, its cross sectioning ability is worse than direct detection. In direct detection the cell nucleus can be easily see while in heterodyne detection we can only see the cell membrane.

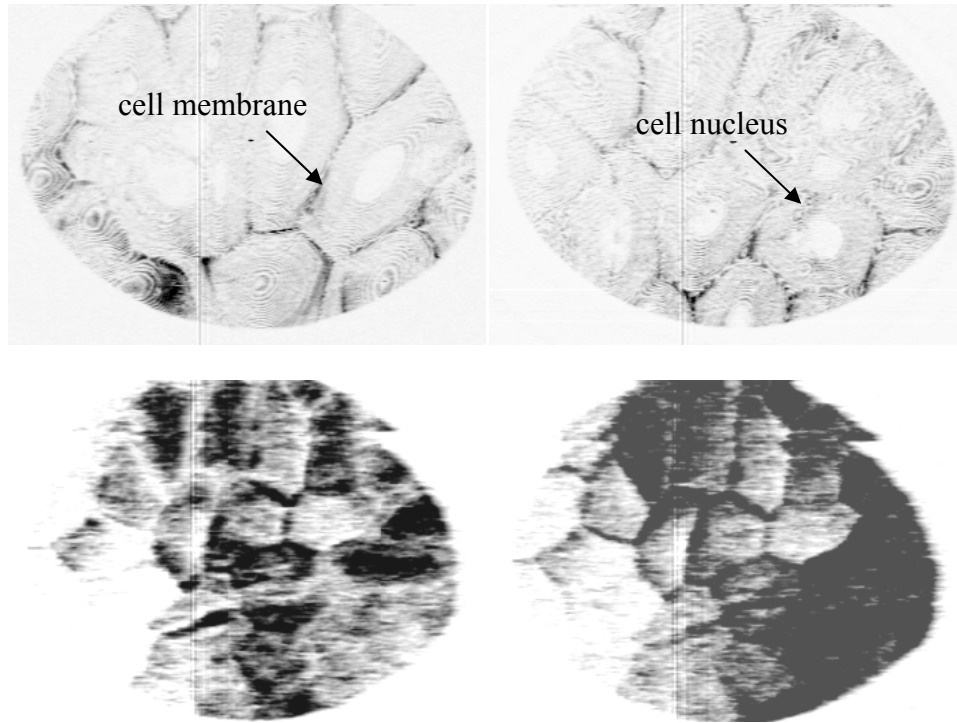


Figure 5.15 Tissue images with direct detection (top) and heterodyne detection (bottom)

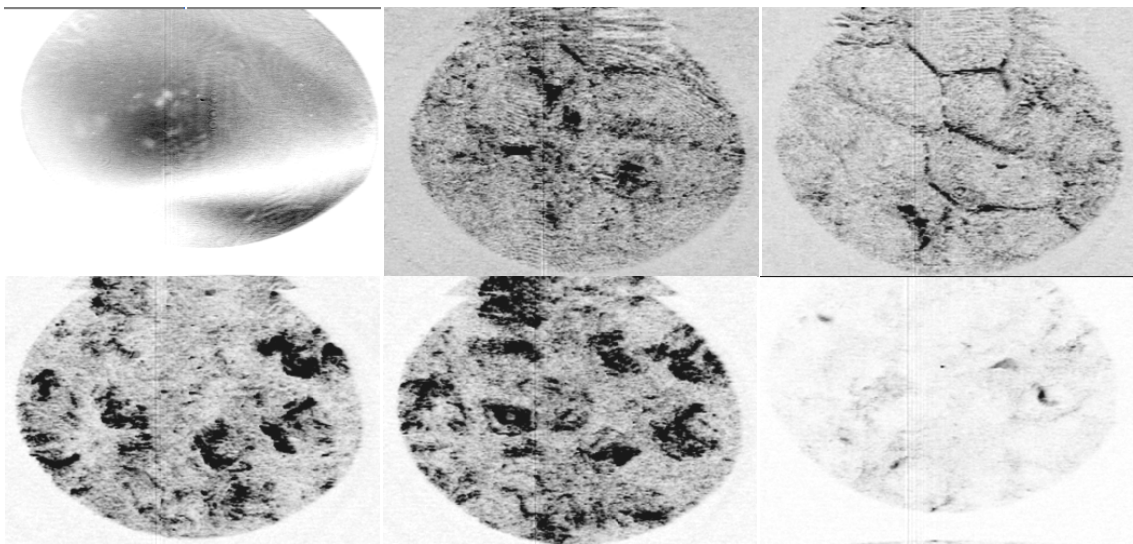


Figure 5.16 Images taken using direct detection at the surface

Figure 5.16 shows images taken using direct detection at the surface, 20μm, 40μm, 60μm, 80μm, 100μm which indicate an approximately 100μm penetration ability.

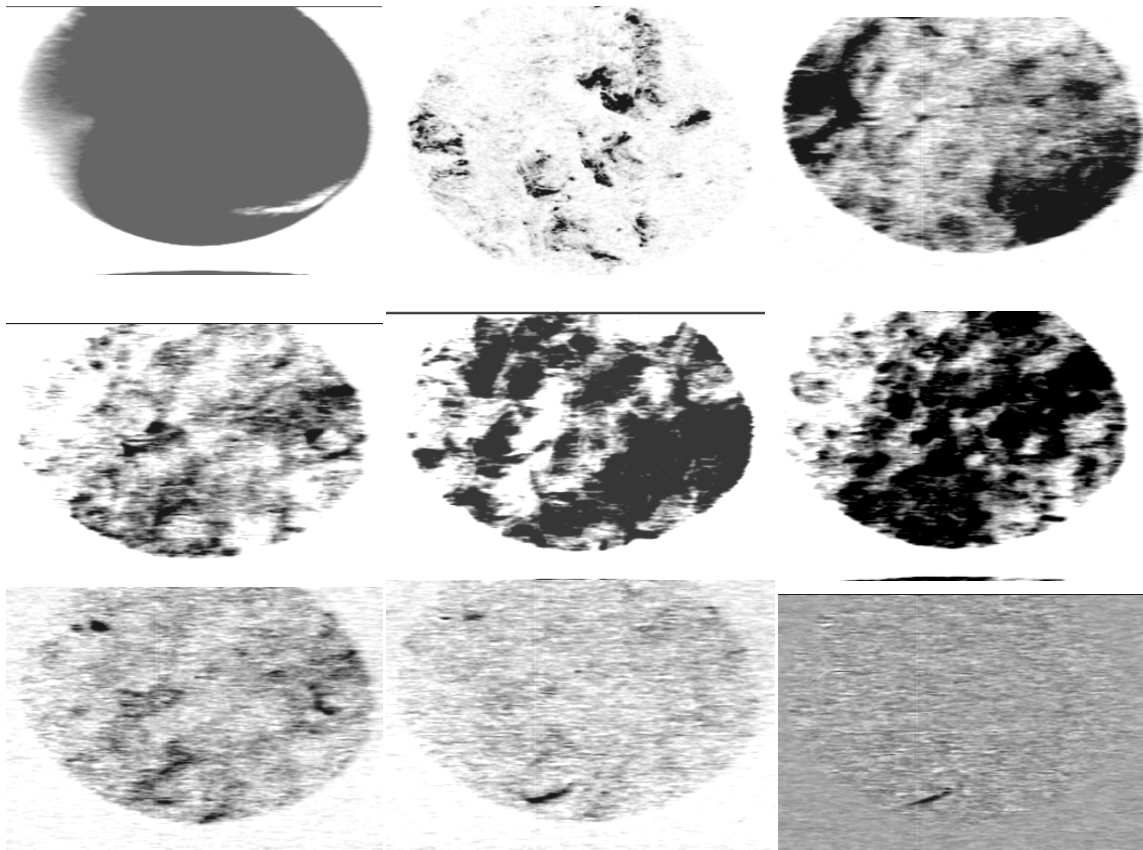


Figure 5.17 Images taken using heterodyne detection at the surface

Figure 5.17 shows Images taken using heterodyne detection at the surface, $20\mu\text{m}$, $40\mu\text{m}$, $60\mu\text{m}$, $80\mu\text{m}$, 100 , $120\mu\text{m}$, $140\mu\text{m}$, $160\mu\text{m}$, which indicate an approximately $160\mu\text{m}$ penetration ability.

The penetration depth of heterodyne detection is about $60\mu\text{m}$ deeper than the penetration depth of direct detection. This matches the improved 30dB dynamic range in heterodyne detection. However, the image quality in heterodyne detection is inferior to the image quality in direct detection. This may be partially explained by the poorer theoretical edge response and axial response in heterodyne detection. Both the minimum resolvable size and cross-sectioning ability are worse in heterodyne detection system. Our

observations also indicate some phase sensitivity due to incomplete recovery of only the amplitude envelope by our electronics, and other imperfections including possible video bandwidth limitations. All of the reasons for the image degradation are not yet fully understood.

CONCLUSION

The existing microscope with direct detection has shown its optical performance to be very close to the theoretical prediction, and its effectiveness has been demonstrated in a clinical setting [14]. The weakness of the direct detection system is that the penetration depth is limited to approximately $100\mu\text{m}$ due to the thermal noise from the detector. In this case, we are not able to detect the skin cancer cells residing beyond that depth. For the purpose of deep penetration, a technique called heterodyne detection is utilized to achieve larger dynamic range and better noise performance.

The most important feature of the heterodyne detection is that in the heterodyne detection system the output signal is proportional to the square root of the intensity of the backscattered light coupled into the fiber while in direct detection the output signal is proportional to the intensity of the light coupled into the fiber. In addition, due to the relatively high carrier frequency, the $1/f$ noise and most narrow-band interference can be minimized. It makes the dominant noise the shot noise which can also be minimized by proper balancing. This method improves more than 30dB in dynamic range so that the heterodyne detection system can penetrate $60\mu\text{m}$ more than the direct detection system in plant tissue samples and human skin.

However, the larger dynamic range and deeper penetration is at the cost of degraded image quality. The feature of the heterodyne detection which improves dynamic range, on the other hand, worsens the optical performance of the system. Both the theoretical and measured results show that both the edge response and axial response in heterodyne detection system are inferior to their counterparts in direct detection. The

edge response relates to the imaging capability and the axial response relates to the cross-sectioning ability. They are both very critical properties to skin tissue imaging.

Despite its better noise performance and deeper penetration, the image quality in heterodyne detection system makes it not as powerful as direct detection system in skin cell diagnosis. However the heterodyne detection still has the room for improvement. The current system is working with a log demodulation detector which helps boost the small signals but has worse edge response and axial response compared with a linear demodulation detector. Although the heterodyne detection system with linear detector has broader edge response and axial response than is achieved with direct detection, it still can penetrate as deep as the system with a log detector and its edge response and axial response may offer a useful compromise. Our demodulation system based on quadrature phase mixing suffered from excessive phase drift, precluding experimental verification of heterodyne imaging with linear amplification.

Other imperfections may contribute to the poor image quality observed in scattering tissue. Drift in the phase reference from the acoustic-optical modulator leads to a variable DC offset in the detected images. This can be improved with a future change to the experimental apparatus to provide an optical pickup of the modulation reference signal. Moreover, the 50/50 coupler is not perfectly splitting the power at our operating wavelength. Although this can be compensated by adjusting one connector of the balanced detector to make the reference power equal, the signal beam is not well balanced. This will make the detector fail to respond when the signals are very small. This can be solved by changing the wavelength of the laser source to 785nm which the

50/50 coupler is manufactured for. By making the improvement above, the heterodyne detection is expected to keep penetrating deeper and have improved images. It is unknown whether these improvements will result in images that are comparable in quality to the images obtained using direct detection.

Future Work

The main advantage of the heterodyne system is its excellent noise performance. In our system, although the heterodyne detection system exceeds the direct detection system in noise performance, it does not offer excellent imaging capability. This is due to the nature of the heterodyne detection with log detector, unwanted optical reflection from the optical component in the system, and suboptimal balancing in the fiber coupler. These problems can be solved with further engineering improvements. In addition, focus control using a MEMS control mirror will be integrated into this imaging system to get rid of the mechanical focus control translation stage in order to increase the mechanical simplicity and accuracy of the system, and provide a path toward further miniaturization. Also, the MEMS mirror will provide some compensation of spherical aberration, which may be critical for deep penetration imaging. Finally, we would like to change this bench-top system to a portable one like the existing handheld CLSM, which makes it more useful under a clinical setting.

REFERENCES CITED

- [1] "Sun Protection." National Cancer Institute's Cancer Trends Progress Report - 2007 Update. 15 April 2008.
- [2] Howard W. Rogers, MD, PhD, Martin A. Weinstock, MD, PhD, et al. Incidence Estimate of Non-melanoma Skin Cancer in the United States, 2006. *Archives of Dermatology* 2010.
- [3] American Cancer Society. *Cancer Facts & Figures 2009*. Atlanta: American Cancer Society; 2009.
- [4] Jamaica Cancer Society. <http://www.jamaicacancersociety.org/pages/skincancer.htm>
- [5] "Squamous Cell Carcinoma." *American Academy of Dermatology*, 15 April 2008.
- [6] S. Presser, J. Taylor. Clinical diagnostic accuracy of basal cell carcinoma. *Journal of the American Academy of Dermatology*, 16:988990, 1987.
- [7] Nikon MicroscopyU. <http://www.microscopyu.com/tutorials/java/virtual/confocal/index.html>
- [8] Wikipedia. http://en.wikipedia.org/wiki/Optical_coherence_tomography
- [9] C.L Arrasmith. A combined confocal imaging and Raman spectroscopy microscope for in vivo skin cancer diagnosis, Montana State University, 2008
- [10] Newport. Datasheet for F-PMC-780-50 polarization maintaining coupler
- [11] C. D. Motchenbacher , J. A. Connelly. *Low Noise Electronic System Design*, WileyInterscience, 1993
- [12] M. Gu, C. J. R. Sheppard, X. Gan. Image formation in a fiber-optical confocal scanning microscope. *Journal of the Optical Society of America A*, 8:1755-1761 , November 1991.
- [13] D. L. Dickensheets. A microfabricated scanning confocal optical microscope for in situ imaging. Doctoral Dissertation, Stanford University, 1997
- [14] Christopher L. Arrasmith, David L. Dickensheets, and Anita Mahadevan-Jansen, "MEMS-based handheld confocal microscope for in-vivo skin imaging," *Opt. Express* 18, 3805-3819 (2010)